A Multi-omic Atlas of Human Choroid Plexus in Alzheimer's Disease

Tristan J. Philippe[1], Denis R. Avey [1,2], Nicola A. Kearns [1,2], Himanshu Vyas[1], Sashini De Tissera[1], Jishu Xu[1], Bernard Ng[1], Devin M. Saunders[1], Amiko K. Lagrimas[1], Duc Duong[3], Nicholas T. Seyfried[3], David A. Bennett[1,2], Yanling Wang[1,2]

1. Rush Alzheimer's Disease Center, Rush University Medical Center, Chicago, IL, 60612, USA
2. Department of Neurological Sciences, Rush University Medical Center, Chicago, IL, 60612, USA
3. Emory University School of Medicine, Atlanta, GA 30322, USA

*Correspondence to Yanling_Wang@rush.edu

Abstract

The choroid plexus (CP) regulates barrier integrity, cerebrospinal-fluid (CSF) dynamics, and immune surveillance, yet its role in Alzheimer's disease (AD) remains poorly defined. We performed snRNA-seq on CP samples from 69 ROSMAP participants spanning normal cognition, mild cognitive impairment, and AD dementia, and integrated these data with spatial transcriptomics, snATAC-seq, and proteomics from CP tissue and CSF. We identified 17 CP cell states and uncovered widespread disease-associated transitions that converged into three major phenotypic axes. Along the inflammatory axis, epithelial cells and border-associated macrophages (BAMs) showed progressive immune activation, with BAMs shifting from inflammatory to stress-dominant states. In the barrier axis, epithelial cells, fibroblasts, and endothelial cells exhibited reduced junction-related gene expression and broad alterations in transport pathways. Epithelial cells also showed late-stage cilia loss and CSF-regulatory pathway impairment, indicating a breakdown in epithelial polarity and CSF sensing, consistent with abnormal CSF proteomic signatures. Along the remodeling axis, fibroblasts showed ECM alterations, while epithelial and stromal cells demonstrated aberrant cell–matrix adhesion pathways. Spatial neighborhood analysis revealed a multicellular signaling hub, with epithelial-rich niches showing the strongest dysregulation in AD. Together, these findings define a unified model of CP dysfunction in AD and position the CP as an active, multicellular contributor to AD pathophysiology.

Introduction

The choroid plexus (CP) has traditionally been viewed as a supporting structure that forms the interface between the brain and periphery, producing cerebrospinal fluid (CSF). However, emerging evidence suggests that the CP is a dynamic regulator of brain homeostasis, modulating barrier permeability, molecular transport, metabolism, and immune surveillance[1–4]. Disruption of CP function has been implicated in impaired CSF flow, barrier breakdown, and neuroinflammation—processes that are highly relevant to Alzheimer's disease (AD)[5–7].

Despite these links, the CP has received considerably less attention in AD research than the brain parenchyma. Studies using animal models or human tissue suggest that CP barrier integrity and function are altered in AD, potentially affecting immune cell trafficking and the clearance of pathological proteins[8–15]. However, a comprehensive understanding of how human CP cell states shift along the clinical continuum from no cognitive impairment (NCI) to mild cognitive impairment (MCI) and Alzheimer's dementia (ADd) remains lacking.

To address this gap, we applied high-resolution single-cell multi-omics and spatial transcriptomics to construct a detailed atlas of CP alterations across NCI, MCI, and ADd individuals from the Religious Orders Study or Rush Memory and Aging Project (ROSMAP)[16]. Our analysis reveals coordinated cell state differences in epithelial, immune, endothelial, and fibroblast populations that collectively reshape the CP's immune, barrier, and stromal landscape during disease progression, offering new mechanistic insights into how CP dysfunction contributes to AD pathophysiology.

Results

Major cell classes of the human choroid plexus

To transcriptionally characterize the CP cell types and states, we performed snRNA-seq on 69 individuals (NCI=21, MCI=21, and ADd=27; Fig. 1a-b; Extended Data table 1). After quality control and doublet removal, we recovered 758,302 total nuclei. Based on canonical markers, we annotated cell clusters and detected five major CP cell types, including epithelial (*HTR2C, CLIC6, CFAP54, DNAH11*), fibroblast (*DCN*, *LEPR*, *FN1*), endothelial (*PECAM1*, *VWF*, *INSR*), mural (*ACTA2*, *TAGLN*, *MYH11*), and immune (*CD163*, *STAB1*, *MSR1*) populations (Fig. 1c–d, Extended Data table 2). Gene detection per nucleus was consistent with previous postmortem human snRNA-seq studies[18–20] (Extended Data Fig. 1a-c), and no significant cell-type proportion differences were observed between NCI, MCI and ADd groups (Fig. 1e Extended Data table 3).

We next validated the major CP cell types by multiplex immunohistochemistry. Consistent with previous human histological studies[21], we detected TTR^+ epithelial cells forming the luminal boundary, DCN^+ fibroblasts

enriched in stromal regions, CD31/PECAM1$^+$ endothelial cells comprising small and large vessels, SMA$^+$ mural cells constituting the large vessel wall, and CD45$^+$ immune cells dispersed across stromal and epithelial compartments (Fig. 1f). Together, these results confirm the identity of major CP cell types and highlight the widespread presence of immune cells across stromal and vascular compartments.

To validate marker gene expression and spatially contextualize these findings, we applied spatial gene profiling using the CosMx Spatial Molecular Imager on CP sections from eight individuals (NCI=4; AD=4; Extended Data table 1, Fig 1i, upper left) with the 6K human discovery panel. After excluding low-quality or mis-segmented cells, we obtained 106,556 high-quality cells for analysis. Unbiased clustering and annotation revealed the same major CP cell types identified in snRNA-seq (Fig. 1g, Extended Data Fig 1d-i, Extended Data table 4), with no significant differences in cell-type proportions between NCI and AD (Fig. 1h, Extended Data table 5). We confirmed the expected localization of annotated cell types, including epithelial, fibroblast, endothelial, mural, and immune cells (Fig. 1i, top). At the gene level, canonical markers were enriched in their expected cell types: *TTR*, *HTR2C*, and *GPX3* in epithelial cells; *DCN*, *FN1*, and *LEPR* in fibroblasts; *VWF*, *PECAM1*, and *INSR* in endothelial cells; *MYH11*, *TAGLN*, and *ACTA2* in mural cells; and *STAB1*, *CD163*, and *MSR1* in immune cells (Fig. 1i, bottom). These data validate cell-type assignments and demonstrate the spatial organization of CP cellular compartments.

We conducted multi-omic profiling (snATAC-seq with matched snRNA-seq) in a subset of cases (n=6) to assess chromatin accessibility alongside gene expression. After standard QC, UMAP clustering identified major epithelial, fibroblast and immune clusters, with ATAC accessibility patterns concordant with RNA-based cell type assignments (Extended Data Fig. k-q, Extended Data table 6).

Epithelial cells exhibit progressive inflammatory activation and late ciliary dysfunction in the choroid plexus across disease stages

We subclustered CP epithelial cells into four transcriptionally distinct epithelial subtypes: Epi_1a, Epi_1b, Epi_2a, and Epi_2b (Fig. 2a-e, Extended Data Fig. 2a-d, and tables 7-9). Epi_2a/2b were enriched for transport and secretory genes (*TTR*, *AQP1*, *SLC25A6*, *SLC25A23*, *SLC4A2*), and Epi_1a/1b/2a were enriched for ciliogenesis signatures (*DNAH6*, *CFAP100*, *CFAP69*). Epi_2a/2b showed higher tight-junction proteins (*CLDN1/5*, *OCLN*) and greater mitochondrial gene expression (*MT-CO1*, *MT-CO2*, *MT-CO3*) (Fig. 2b, Extended Data table 7). Functional annotation further aligned with marker gene profiles: Epi_1a/1b and Epi_1b/2a were associated with microtubule movement and cilium assembly, and Epi_2b was enriched for transport and metabolic processes (Fig. 2c).

Unsupervised clustering across spatial transcriptomics (ST) and ATAC-seq consistently identified four major

118 epithelial subclusters (Fig. 2d, Extended data Table 8; Extended Data Fig. 2a-d and Table 8-9). Although
119 individual marker genes showed variable assignments across data types, likely reflecting modality-specific
120 resolution, we identified both ciliated and less-ciliated cell states within epithelial cells (Fig. 2d–e, Extended
121 Data Table 8-9; Extended Data Fig. 2a-d).
122
123 Importantly, the relative proportions of the four epithelial subclusters were stable across NCI, MCI, and ADd in
124 our snRNA-seq and ST data (Fig. 2f-g, Extended Data Table 3 and 5), indicating that epithelial heterogeneity
125 itself is not disease-associated. We next examined transcriptome differences across AD disease progression at
126 both the aggregated epithelial cell level and within individual epithelial subtypes. Along the disease trajectory
127 from NCI to MCI to ADd, we detected progressive upregulation of immune and inflammatory genes (e.g. *IL6R*
128 and *SERPINE3*). However, we observed a marked downregulation of cilia-related genes (e.g. *CROCC*, *FOXJ1*,
129 *TUBA1A*, and *CFAP43*) that correlated with cognitive decline (Extended Data Fig. 2e and Table 10-11). Gene
130 set enrichment analysis revealed that immune responses, secretion, and transporter activities were progressively
131 higher from NCI to ADd, whereas cilia-related pathways were selectively lower in ADd (Fig. 2h). At the
132 epithelial subtype level, Epi_1b/2a carried the strongest signatures of both immune activation and cilia loss
133 (Fig. 2h). ST corroborated these findings at the aggregated epithelial cell level (Fig 2h right and Extended Data
134 Table 12).
135
136 To resolve disease temporal patterns, we used template matching[22] to classify disease-associated transcriptional
137 programs into different patterns and identified two major categories: progressive differences included immune
138 and transporter genes (e.g., *SLC17A5*, *IL6R*; Fig. 2i), while late-stage changes were dominated by cilia-related
139 genes (*CROCC*, *FOXJ1*, *TUBA4A*; Fig. 2i and Extended Data Table 10). ST corroborated these findings,
140 revealing reduced cilia gene expression (*FOXJ1*, *TUBA4A*) in ADd epithelium (Fig. 2j). Chromatin accessibility
141 profiling by snATAC-seq further validated these observations, showing less accessibility at key cilia-related
142 transcription factor loci (e.g. *FOXJ1, KLF4)*) and correspondingly structural gene loci (*CROCC,*
143 *DYNC1H1* and *TUBA4A*), consistent with their transcriptional downregulation (Fig. 2k, Extended Data Table
144 13). Immunohistochemistry confirmed a reduction of ciliary rootlets, with CROCC staining markedly lower in
145 AD relative to controls (Fig. 2l).
146
147 Since the CP epithelium is a key tissue interface with CSF, we next examined protein expression in CSF using
148 the Olink Explore platform (n=27), which enabled measurement of 2,884 proteins (Fig. 2m, upper). This
149 analysis revealed stage-dependent differences that paralleled the transcriptomic findings. At the early stage of
150 AD progression, we observed more inflammatory signatures, including enrichment of monocyte chemotaxis and
151 chemokine activity pathways (Fig. 2m). By the late stage, we detected lower cilium-related terms and multiple
152 changes to metabolic processes, including proteasomal and collagen catabolism (Fig. 2m; Extended Data Table

153 14). Together, these data highlight coordinated molecular changes between CP epithelial cells and the CSF
154 proteome, reinforcing the role of the CP as a dynamic interface linking inflammation and impaired CSF
155 secretion mechanisms in AD.
156
157 **Border-associated macrophages shifted from inflammatory to stress-associated states in the choroid**
158 **plexus across disease stages**
159 We next examined immune cells in the CP. Multiplex fluorescent imaging confirmed the presence of $CD163^+$
160 macrophages and $CD3^+$ T cells within the ECAD+ CP tissue (Fig. 3a). Subclustering of snRNA-seq data
161 identified three states of border-associated macrophages (BAM_1-3) and a small T-cell population marked by
162 expression of *THEMIS* and *CD3E* (Fig. 3b). BAM_1 expressed *CD163*, *MRC1*, *LYVE1*, and *IL4R*, consistent
163 with an immune-activated state. BAM_2 was enriched for heat-shock protein genes (*HSPE1*, -, *HSPA8,*
164 *DNAJA1*), indicative of a stress-adapted phenotype, while BAM_3 expressed *MKI67* and *CENPF*, reflecting a
165 proliferative subset. Functional enrichment supported these distinctions: BAM_1 was associated with immune
166 activation and cytokine release, BAM_2 with protein folding and stress responses, and BAM_3 with cell cycle
167 and proliferation (Fig. 3c-d, Extended Data Table 15). snATAC-seq revealed selective chromatin accessibility
168 at *DNAJA1* and *HSPA8* loci within the BAM2 subcluster, consistent with their elevated transcription (Fig. 3e,
169 Extended Data Fig. 3a-b and Table 16). Notably, BAM1- and BAM2-specific transcriptional signatures
170 corresponded with distinct ATAC activity, indicating coordinated regulation of chromatin accessibility and
171 gene expression across BAM states (Fig. 3f). Because of limited immune cell numbers, we applied a supervised
172 approach[23] to annotate ST subclusters, which showed strong correspondence with snRNA-seq–defined BAM
173 populations (Fig. 3g-h, Extended data Fig 3c). When mapped back to the CP, BAM1, BAM2, BAM3, and T
174 cells were broadly distributed, confirming the presence of these immune populations throughout the tissue (Fig.
175 3h).
176
177 Notably, we observed higher BAM_2 proportions in ADd (Fig. 3i, Extended Data Table 3), indicating a shifted
178 state toward a stress-dominant phenotype. At the pathway level, we observed progressively stronger immune
179 responses across disease stages, including enrichment of pathways such as antigen presentation, leukocyte
180 proliferation, and other signatures of immune activation. In ADd, we also detected enrichment of unfolded
181 protein binding, indicative of stress responses, consistent with the expansion of the BAM_2 population
182 characterized by high expression of heat shock proteins (Fig. 3j). At the gene level, we observed stage-
183 dependent regulation of classical immune-related genes, including *HLA-DRA*, as well as additional immune-
184 associated genes linked to CP function, such as *CDC42SE1*, *LY75*, *TRIM14*, and *MR1* in early stages,
185 and *LPAR1*, *TNFAIP2*, *CDC42*, and *HSPA1*A in late stages (Fig. 3k, Extended Data Table 17). Spatial
186 transcriptomics data confirmed increased *HSP* expression, along with

elevated *CD68* and *HLA-DRA/DRB* expression in AD (Fig. 3j, right and l-m, Extended Data Table 18). Immunostaining further validated these findings, showing higher HLA-DR and CD68 intensity in CD163$^+$ macrophages in AD compared with NCI (Fig. 3n). However, we did not observe significant differences in the number of total T cells, CD4$^+$ T cells, or CD8$^+$ cells in AD (Fig. 3o, Extended Data Fig. 3d). Together, these results demonstrate that immune cells in the CP are heterogeneous and undergo progressive immune activation and stress responses across disease stages.

Fibroblast remodeling in the choroid plexus in AD dementia

To characterize fibroblast heterogeneity in the CP, we subclustered fibroblasts into three transcriptional subtypes (Fib_1, Fib_2, Fib_3; Fig. 4a). Fib_1 expressed markers such as *LEPR*, *PLXNA4*, and *STXBP6*, consistent with regulatory and signaling functions. Fib_2 was enriched for *CLDN11*, *TJP1, ITGBL1, GJB6, TRPM3*, and *ROBO1*, indicative of tight-junction-expressing barrier-like fibroblasts. Fib_3 expressed *DCN*, *FN1*, *FBLN1*, *CDH11*, and multiple collagens (e.g., *COL4A2*, *COL3A1*, *COL6A3*), indicative of extracellular-matrix (ECM)-producing fibroblasts (Fig. 4b, Extended Data Table 19). Recent work identified a population of "base barrier" fibroblasts in the mouse CP using scRNA-seq[2], describing them as a barrier-forming population at the stroma–CSF interface. While similar gene signatures were noted in a published human dataset[19], those base barrier fibroblasts had not been independently resolved in human tissue due to limited sampling. Our study extends these findings using unbiased clustering of a larger cohort, resolving Fibro_2 as the human counterpart of this base barrier fibroblast population. Immunohistochemistry staining confirmed that CLDN11$^+$ Fibro_2 localized to the basal side of the CP epithelium, particularly around larger vessels (CD31, SMA) adjacent to the brain parenchyma, consistent with a barrier-supporting niche (Fig. 4c).

Despite these molecular distinctions, gene ontology enrichment showed broad overlap across fibroblast subtypes, with shared programs in adhesion, ECM organization, and ion transport (Extended Data Fig. 4a).We then applied the same supervised approach[23] to annotate ST fibroblast subclusters, which showed modest correspondence with snRNA-seq–defined populations (Extended Data Fig. 4b; Fig. 4d) and mapped to original locations within the CP (Fig. 4e).

We next examined disease-associated transcriptional differences at the fibroblast subtype level. Fibroblast proportions were similar across NCI, MCI, and ADd (Fig. 4f), indicating that disease progression does not alter relative abundance but instead drives transcriptional reprogramming within each subtype. Gene set enrichment analyses revealed broad transcriptional reprogramming across major pathways, with changes most pronounced at the late stage (Fig. 4g and Extended Data Table 20-21). Tight junction-related pathways showed overall negative enrichment, indicating weakened barrier integrity. By contrast, pathways related to cell–matrix adhesion, transporter, and ion channel pathways displayed positive enrichment at the late stage, indicating an

222 adaptive transcriptional response. Among fibroblast subtypes, Fibro_2 showed the most consistent upregulation
223 of ECM- and transporter-related pathways. At the tissue level, ST data revealed a general downregulation of
224 transporter and ion channel activity and upregulation of ECM remodeling. We observed that pathway
225 directionality is not always concordant between snRNA-seq and ST, likely reflecting differences in cell-type
226 purity, spatial mixing within ST spots, and modality-specific sensitivity to fibroblast state composition.
227 Together, these findings indicate that fibroblast remodeling in ADd involves broad transcriptional changes, with
228 consistent tight junction weakening and ECM remodeling.
229
230 To further resolve temporal differences, we examined gene expression patterns in fibroblasts. Several collagen-
231 related genes, including *ADAMTS9*, *COL15A1*, and *LAMA2*, were progressively upregulated, consistent with
232 greater ECM deposition, whereas others, such as *COL8A1*, were downregulated, indicating selective collagen
233 loss (Fig. 4h Extended Data Fig. 4c). Similarly, transporter genes, such as the SLC family (*SLC25A8*, *SLC16A4*,
234 *SLC16A9*), also exhibited bidirectional regulation, highlighting heterogeneous shifts in ion and metabolite
235 handling. To examine stage-dependent transcriptional dynamics, we compared differentially expressed genes
236 (DEGs) across fibroblast subtypes at each disease stage. The overlap between DEGs across stages was mild to
237 moderate, suggesting progressive but partly distinct transcriptional alterations during disease progression.
238 Similarly, when comparing ADd versus NCI across different fibroblast subtypes, only limited overlap was
239 observed, indicating that each fibroblast subtype exhibits partially unique transcriptional responses to AD
240 pathology (Extended Data Fig. 4d-e).
241
242 ST analysis confirmed these fibroblast-specific transcriptional changes in AD, with increased *ADAMTS9*,
243 *COL15A1*, and *LAMA2* expression and reduced *COL8A1* relative to controls (Fig. 4i). To validate these findings
244 at the histological level, we performed Movat's pentachrome staining, followed by color deconvolution and
245 ECM threshold masking to quantify collagen deposition (Fig. 4j). The density distribution analysis revealed a
246 subtle shift from low- to high-collagen regions in AD and MCI compared with NCI although this trend did not
247 reach statistical significance (Fig. 4j).
248
249 **Endothelial and mural cell dysregulation in the choroid plexus in AD dementia**
250 We next investigated vascular compartments of the CP, focusing on endothelial and mural cells. We identified
251 three endothelial subtypes (Endo_1, Endo_2, Endo_3) and three mural subtypes (Mural_1, Mural_2, Mural_3.
252 Endo_1 was characterized by strong *PECAM1*, *CLDN5*, and *CDH13* expression with lower *VWF*, consistent
253 with an arterial/arteriolar endothelial identity. Endo_2 also expressed *CLDN5* but showed higher *VWF* together
254 with *CEMIP2*, *IL1R1*, and *IL4R*, consistent with a venous endothelial phenotype. Endo_3 was distinguished by
255 robust *PLVAP* and *FLT1* expression, consistent with fenestrated capillary endothelium in the CP (Fig 5a-b,
256 Extended Data Table 22). Mural_1 expressed high levels of canonical contractile smooth muscle markers,

including *ACTA2*, *MYH11*, *TPM1*, and *MYOCD*, consistent with arterial smooth muscle cells. Mural_2 showed lower expression of contractile genes but enrichment of ECM-remodeling transcripts such as *COL18A1*, *ADAMTS9*, and *CRISPLD2*, indicative of a venous smooth muscle or transitional phenotype. Mural_3 exhibited reduced expression of smooth muscle genes and upregulation of signaling and matrix regulators such as *CEMIP*, *PLXDC2*, and *ENPP2*, consistent with a pericyte identity associated with capillaries (Fig 5c-d, Extended Data Table 23). We then applied the same supervised approach[23] to identify ST vascular subtypes, which showed strong correspondence with snRNA-seq–defined populations (Fig. 5e) and mapped to vascular niches within the CP (Fig. 5g).

We next asked how mural subtypes are positioned relative to endothelial populations (Fig. 5f). Mural_1, which we annotated as arterial smooth muscle cells, was preferentially associated with Endo_1 (arterial endothelium). By contrast, Mural_3, defined as pericytes, showed enrichment near Endo_3, corresponding to fenestrated capillary endothelium. These relationships indicate coordinated arterial and capillary compartmentalization between endothelial and mural cells in the choroid plexus.

To validate the endothelial subtype classification, we performed immunostaining with CLDN5 and PLVAP together with SMA and CAV to visualize vascular structure (Fig. 5h). CLDN5 was strongly expressed in arteries and veins, whereas PLVAP was selectively enriched in capillaries. Arteries and veins were further distinguished by mural SMA staining, with arteries showing thick, robust expression and veins exhibiting thinner signals. These findings confirmed that CLDN5 and PLVAP are reliable markers for distinguishing arterial/venous from capillary endothelial cells. The endothelial cell representation did not differ across NCI, MCI, and ADd groups, whereas mural populations had a lower Mural_3 subtype in ADd (Fig. 5i). Given the pericyte-like transcriptional profile of Mural_3, this decrease may reflect pericyte loss or dedifferentiation, indicating vascular instability and barrier dysfunction in ADd. Correspondingly, differential expression analyses in snRNA-seq and ST revealed progressive reductions in junctional and actin-binding pathways, along with downregulation of ion transport signatures, consistent with progressive barrier weakening in ADd (Extended Data Tables 24-27).

Transcriptomic–proteomic concordance highlights multicellular dysfunction in the choroid plexus in AD dementia

To determine whether cell type–specific transcriptomic changes are mirrored at the protein level, we compared snRNA-seq–derived differential gene signatures (ADd vs. NCI) across major cell types with bulk CP proteomic profiles stratified by disease stage (Fig. 5j, Extended Data Table 28). Transcriptionally, BAM cells showed strong immune activation, including enrichment of antigen presentation, leukocyte proliferation, and inflammatory pathways, with immune-associated changes also evident at the protein level at late stage (AD vs.

292 MCI). In epithelial cells, transcriptional analyses revealed downregulation of cilia-related pathways, which was
293 consistent with corresponding protein-level reductions in ADd. More broadly, transcriptional remodeling of
294 barrier- and transport-associated programs—including tight junctions, extracellular matrix, cell adhesion, and
295 ion/transport channels, was observed across fibroblast, endothelial, mural, and epithelial compartments, with
296 these pathway classes likewise implicated in stage-associated proteomic remodeling. Together, these findings
297 highlight three convergent molecular signatures of CP dysfunction during AD progression: BAM immune
298 activation, broad remodeling of junctional, adhesion, ECM, and transport pathways, and cilia reduction.
299
300 **Inferred intercellular communication changes in the choroid plexus in AD dementia**
301 To assess differences in intercellular signaling, we applied CellChat[24] to snRNA-seq data to infer ligand–
302 receptor–mediated communication. ADd cases showed higher weights of interactions compared with controls
303 (Fig. 6a, number of interactions: Extended data Fig 5a). These increases were largely driven by differences in
304 communication among fibroblasts, endothelial, immune, and mural cells through ECM-related pathways,
305 including Collagen, Laminin, BMP, JAM, EPHA, and FN1 (Fig. 6b, Extended data Fig 5b-d, and Table 29).
306
307 Because the CP is organized into stromal, vascular, and epithelial compartments, spatial context is essential for
308 interpreting AD-related differences. We therefore performed nearest-neighbor analysis on spatial
309 transcriptomics data to define local microenvironments ("niches"). Each neighborhood matrix was constructed
310 by averaging expression across a random 10-cell subset of the 25 nearest neighbors, which revealed three
311 spatial niches (Fig. 6c-d, Extended data Fig. 6a-d): niche 1 corresponded to vessel-rich stroma (fibroblasts,
312 endothelial, mural cells), niche 3 was enriched for epithelial cells, and niche 2 represented an intermediate
313 epithelial environment (Extended data Fig. 6e). Spatial mapping confirmed this organization, with niche 1
314 localized near vessels and niche 3 closer to the epithelium, which also showed the highest expression
315 of *TTR* (Fig. 6e-f; Extended data Fig. 6f). Examination of subtype distributions across niches revealed niche-
316 specific enrichment of certain immune, fibroblast, and epithelial subtypes (Extended data Fig. 6g). Gene set
317 enrichment reflected these differences: niche 1 was enriched for immune activation, inflammation, vasculature,
318 and ECM remodeling, while niche 3 was associated with metabolism, oxidative stress, autophagy, transport,
319 and cilia (Fig. 6h).
320
321 We next applied CellChat analysis to the spatial transcriptomic data to resolve AD-associated signaling
322 alterations across all cells and within defined spatial niches. Consistent with single-nucleus findings, overall
323 cell–cell communication probabilities were higher in AD, particularly within niche 3 (Fig. 6g; Extended data
324 Fig. 6h). Across niches, the most upregulated pathways in AD involved APP-, APOE-, and ECM-related
325 signaling (e.g., COLLAGEN, LAMININ, FN1, THBS), immune/inflammatory (MIF, CXCL), as well as growth
326 factor–mediated networks (FGF, VEGF, PDGF, ADGRG), indicating widespread matrix remodeling and

327 paracrine activation (Fig. 6i; Extended data Table 29). At the cell-type level, niche 1 and niche 2 showed more
328 limited pathway activation, with significantly elevated pathways generally involving one or two dominant cell
329 types (Fig. 6j). In contrast, niche 3 exhibited broader pathway activation that frequently involved multiple cell
330 types (Fig. 6j), highlighting its role as a multicellular signaling hub in AD.
331
332 **Discussion**
333
334 By integrating single-nucleus RNA-seq, ATAC-seq and spatial transcriptomic data, we establish a multi-omic
335 atlas for a previously understudied brain border tissue—the human choroid plexus (CP). We defined 17 distinct
336 CP cell states and revealed their molecular remodeling across the disease continuum from normal cognition to
337 AD dementia. Together with proteomic datasets from CP tissue and cerebrospinal fluid, these results provide a
338 publicly accessible, multidimensional resource for investigating CP biology, barrier regulation, and disease-
339 associated remodeling in AD and human aging. Our multi-omic analyses revealed that AD dementia was not
340 characterized by major differences in cell-type composition but by widespread cell-intrinsic transitions that
341 collectively reshaped the CP's immune, barrier, and stromal networks. These transitions converged into three
342 major phenotypic axes —immune activation, barrier disruption, and stromal remodeling—that together define a
343 chronically stressed and progressively compromised CP landscape in AD.
344
345 Along the inflammatory axis, both epithelial cells and border-associated macrophages (BAMs) exhibited
346 progressive inflammatory activation and upregulated T-cell-activation, antigen-presentation, and cytokine-
347 response programs, indicating coordinated immune engagement within the CP. At the late stage, BAMs
348 apparently acquired stress-associated states marked by heat-shock-gene expression, suggesting maladaptive
349 persistence under chronic inflammatory pressure. Consistent with these transcriptomic changes,
350 immunostaining revealed increased $CD68^+$ and $HLA\text{-}DR^+$ macrophages indicating enhanced local macrophage
351 activation. Despite macrophage upregulation of leukocyte-adhesion and antigen-presentation genes, we
352 observed no change in $CD3^+$ T cells—consistent with a sustained but compartmentalized inflammatory response
353 distinct from the leukocyte trafficking phenotype characteristic of acute injury or infection[7,24,25].
354
355 At the barrier level, our analyses revealed broad compromise of cell-junction and adhesion pathways across
356 epithelial, endothelial, and fibroblast compartments. Epithelial cells showed selective downregulation of the
357 tight-junction gene *CLDN5*, while pathway analyses indicated weakening of junctional integrity in secretory
358 epithelial subtypes and endothelial cells, along with a reduction of the Mural_3 pericyte subtype, suggesting
359 progressive loss of vascular support. In addition, fibroblasts—including the putative base-barrier Fibro_2
360 population—displayed lower expression of junctional components, supporting their contribution to barrier
361 maintenance at the stromal–CSF interface. These multicellular alterations were accompanied by aberrant

362 transporter and secretory pathways in epithelial cells along with a marked reduction in cilia function, validated
363 by CROCC immunostaining, indicating impaired mechanosensory feedback control. Because motile and
364 primary cilia help maintain epithelial polarity and barrier regulation through CSF sensing, their loss likely
365 contributes to barrier dysfunction in AD. Consistent with these molecular and structural changes, CSF
366 proteomic profiles revealed elevated inflammatory proteins together with reduced metabolic and ciliary-
367 associated components, reflecting disrupted epithelial function and altered CSF composition in AD.
368
369 Finally, the remodeling axis highlighted extracellular-matrix (ECM) dynamics, reflecting both matrix
370 degradation and restrained fibrotic deposition. Fibroblasts in AD displayed mixed transcriptional signatures of
371 cell–matrix adhesion and collagen-containing ECM organization. Movat staining showed only a mild increase
372 in collagen accumulation, contrasting sharply with the fibrotic scarring and persistent collagen deposition
373 typical of acute injury or infection[26–28]. Other barrier-associated compartments—including epithelial,
374 endothelial, and mural cells—also exhibited aberrant cell–matrix adhesion and extracellular-matrix pathways
375 (Fig. 5j; Fig.6i), consistent with a coordinated structural remodeling rather than fibroblast-specific collagen
376 deposition. These molecular alterations were further supported by proteomic analyses of CP tissue, which
377 revealed parallel changes in ECM-related and adhesion proteins (Fig. 5j). Thus, the CP in AD exhibited a
378 chronic, low-grade remodeling phenotype consistent with a long-term imbalance between matrix synthesis and
379 degradation.
380
381 Taken together, these axes define a unified model of CP dysfunction in Alzheimer's disease, characterized by
382 chronic immune activation, barrier instability with CSF dysregulation, coordinated ECM and tissue remodeling.
383 The coordinated transcriptional changes across epithelial, stromal, vascular, and immune compartments
384 establish a foundation for mechanistic studies linking cilia function, chronic inflammation, and ECM turnover
385 to disrupted CSF homeostasis. Collectively, these findings position the choroid plexus as a dynamic immune–
386 barrier interface in AD, and highlight epithelial cilia maintenance, junctional resilience, and macrophage stress
387 adaptation as conceptual entry points for therapeutic exploration.
388
389
390 **Acknowledgments**
391 We are grateful to those who agreed to donate their brains for research. We thank all the employees at RADC
392 for their support and assistance. This study was supported by NIA grants R01AG074082 and R01AG079223 (to
393 Y.W.) and P30AG10161, P30AG72975, R01AG015819 R01AG017917, and U01AG61356 (to D. A. B.)
394
395 **Authors' contributions**

D.R.A., N.A.K., and S.D.T. designed and optimized snRNA-seq and snATAC-seq. D.R.A. and S.D.T. performed sample preparation and snRNA-seq and snATAC-seq experiments. S.D.T., H.V., and D.R.A conducted spatial transcriptomics (ST) experiments. J.X. performed snRNA-seq and ATAC-seq data pre-processing. T.J.P. performed all snRNA-seq and snATAC-seq data analyses and generated related figures. T.J.P. Performed ST data preprocessing. T.J.P. and D.R.A. conducted ST analyses and generated related figures. N.A.K. contributed to snRNA-seq analyses. H.V., D.S., A.K.L., and N.A.K. performed immunohistochemistry experiments and data analysis. D.D. and N.T.S. generated mass spectrometry proteomics data. B.N. conducted proteomics analysis. T.J.P., D.R.A., and Y.W. wrote the manuscript with input from all co-authors. D.A.B. directed the parent ROSMAP study. Y.W. conceived and supervised the overall project.

Competing interests

The authors declare no competing interests.

Corresponding authors

Correspondence to Yanling Wang (yanling_wang@rush.edu)

Data availability

Sample information, cluster maker genes, and differentially expressed genes are provided in the Supplemental Information. All snRNA-seq, snATAC-seq and spatial transcriptomic data are available at Synapse under accession code syn2580853. ROS/MAP data can be requested by qualified investigators (www.radc.rush.edu).

Code availability

Code for analysis is available at GitHub (https://github.com/Tristan-J-Philippe/Multi-omic_Choroid-Plexus_Alzheimers-Disease).

Online Methods

Tissue collection

Human post-mortem choroid plexus (CP) tissue was collected from the lateral ventricles of 69 participants in the Religious Order Study Rush Memory and Aging Project (ROSMAP)[16]. The tissue was bisected and preserved for snRNA-seq, proteomics, IHC, or spatial transcriptomics. Tissue used for snRNA-seq and proteomics was snap frozen and stored at -80°C whereas tissue for immunostaining and spatial transcriptomics was formalin fixed and paraffin embedded. Clinical diagnostic, pathologic AD and cerebral amyloid angiopathy (CCA) were assessed as previously described[16,29–31]. The Institutional Review Board of Rush University Medical Center approved both studies. All participants signed an informed consent and Anatomic Gift Act.

429 **Nuclei isolation for snRNA-seq**

430 The clinical diagnosis was used to group ADd, MCI, and NCI into batches of 4-6 participants for snRNA-seq
431 (n=69; Fig.1b, Extended Data Table 1); these groups were balanced for age and sex. All procedures were
432 carried out on ice or at 4 °C to minimize RNA degradation, unless otherwise specified. 100 mg frozen CP tissue
433 was minced on dry ice, then thawed in 0.1X lysis buffer (250 mM sucrose, 25 mM KCl, 5 mM MgCl2, 10 mM
434 Tris pH8, 1µM DTT, 15µM actinomycin, 0.2U/µL RNAse inhibitor, 0.01% v/v Triton X-100). Tissue was
435 pressed through a 100µm cell strainer with the back end of a 5mL plunger, rinsing every 30 seconds with 200
436 µL fresh 0.1X lysis buffer for 3 min total per sample. The cell suspension was pelleted at 600g for 4 min (all
437 centrifugation steps were at 4°C), supernatant was removed, and pellets were resuspended in 1.5 mL 1X lysis
438 buffer with 0.1% Triton X-100. Nuclei were homogenized using a Dounce homogenizer (10 times using pestle
439 B) and incubated for 2 min on ice. Nuclei were washed twice: centrifuged at 700g for 4 min and resuspended in
440 1 mL of wash buffer (1.5% BSA, 0.2U/µL RNAse inhibitor in DPBS). Samples were purified by iodixanol
441 gradient (37%, 29%, 25% with sample) centrifugation (13500g, 20min, OptiPrep Sigma) and collected from the
442 29-37% interface, washed once, filtered through a 40 µm cell strainer (Flowmi), and washed again before QC
443 and counting using Trypan blue.

444

445 For barcoding, nuclei (100k in 187.5uL total volume * 2 unique barcodes per sample) were incubated with 4
446 µM of anchor and 4 µM of a unique barcoded oligonucleotide and incubated for 5min (final concentration of 50
447 nM of each; see Nuclei hashing design). Followed by 4 µM co-anchor, mixed by tapping, incubated on ice for 5
448 min, and 3 washes. Hashed nuclei were then combined, diluted to ~40k nuclei in 43.2 µL, and super-loaded
449 (~40k nuclei loaded per lane) onto 4 lanes of 10X Genomics Chip G or Chip J. Libraries were prepared using
450 the 10x Genomics 3' single-cell gene expression assay v3.1 (CG000317 Rev C) for snRNA-seq alone and
451 (CG000338) for single nuclei RNA and ATAC sequencing except as detailed in method: Nuclei hashtag,
452 followed by sequencing on a NovaSeq 6000 to an average read depth of 50k RNA reads/cell and 15k hash
453 reads/cell.

454

455 **Nuclei hashtag oligonucleotide design and library preparation**

456 Nuclei were barcoded using a modified MULTI-seq[32] protocol to enable pooling and super-loading of the 10X
457 chip. The Anchor sequence was: /5Chol-
458 TEG/GTAACGATCCAGCTGTCACTAGATCGGAAGAGCACACGTCTG, where '5Chol-TEG' denotes a 5'
459 Cholesterol modification conjugated via a triethylene glycol linker. The Co-Anchor sequence was:
460 AGTGACAGCTGGATCGTTAC/3CholTEG/. Sixteen barcoded oligonucleotides (aka "hashtag oligos") were
461 designed following the pattern R2-BC-poly(A), where R2 was a constant partial Read 2 sequence
462 (CAGACGTGTGCTCTTCCGATCT), BC was a unique sample-specific 15-nt barcode sequence (sequences
463 listed below), and poly(A) was a 30-nt poly(A) sequence. The poly(A) enables recovery of hashtag oligos along

with mRNA following reverse transcription. To further enrich for hashtag oligos, a Truseq 2 primer (CAGACGTGTGCTCTTCCGATC) was spiked into the cDNA amplification reaction (CG000317 Rev C step 2.2) at 100 nM. All oligonucleotides were ordered from IDT. For the hashtag library sample index PCR (step 3.5), the reaction consisted of 50 µl Amp mix, 40 µl EB buffer, 5 µl cDNA from transferred supernatant cleanup (step 2.3B), and 5 µl dual index from plate TT. PCR was run for 9 cycles with default settings, followed by a 1.2X SPRI cleanup. Next, 20 ng (~1 µl) of PCR product was used for an additional sample index PCR (6 cycles) to enrich for full-length product. The reaction also consisted of 30 µl Amp mix, 1.2 µl each of Illumina P5 and P7 primers (10 µM), and EB buffer to a total volume of 60 µl. This was followed by one 0.9X SPRI cleanup to remove free primer and primer dimer. The hashtag (HT) libraries (~242-bp total size) were mixed with GEX libraries (ensuring distinct TT indices) at a molar ratio of 1:6 HT:GEX in the final pool to achieve the desired ~1:3 ratio of sequencing reads.

Sample barcodes:

AAGGCAGACGGTGCA

GGCTGCGCACCGCCT

GACGCGCGTTGTCAT

GAAGAAGCGTTATTC

AGAGCTAGGATCGGA

GCTAGCGTAATGTGG

CGGTTAGCGCGGTTC

AGGCGTGCACGTGGT

CACATATAGAATTAG

ATAGCGGCTCTATCG

AGCGCATAGTTATCT

CAGGTCGGCCAAGAT

GCCAAGATCAGGTCC

TAGGTTACGAGTGTG

ATAATCATTACGTGG

ATCGAACCGACAGAG

Spatial transcriptomics of CP using Nanostring CosMx

Eight human CP samples were selected (4 NCI, 4 AD), matched for sex, and balanced for age. 5-µm thick FFPE sections were mounted on Leica BOND Plus microscope slides (4 sections per slide; 2 slides total), ensuring that the tissue resided within the 15x20mm imaging area. Slide preparation followed the manufacturer's protocol (Nanostring MAN10159-03) with the following modifications. Antigen retrieval was carried out using

498 a steamer for 15 min once the retrieval solution reached 99°C. Tissue permeabilization was performed for 15
499 min at 40°C using 3 µg/mL Proteinase K. Probe hybridization occurred for 18 hr at 37°C.
500
501 Primary antibodies included Cell Segmentation Mix 1 (CD298/B2M), Marker Mix 1 (PanCK/CD45), and
502 Marker Mix 2 (CD68) at the recommended dilutions and were incubated for 90 min (instead of 60 min) at room
503 temperature. To load slides on the Nanostring CosMx instrument, we followed the Instrument User Manual
504 (MAN-10161-03-2; software version 1.2) using configuration B for pre-bleaching and configuration A for cell
505 segmentation. Field of view (FOV) selection encompassed the entire tissue-covered area.
506
507 **TMT-based proteomics of choroid plexus tissue**
508 A subset of choroid plexus samples (n = 16; Extended Data Table 1), balanced for age and sex, were analyzed
509 by mass spectrometry. Briefly, tissues were lysed in 8 M urea, 100 mM Tris, 100 mM NaH_2PO_4 (pH 8.5) with
510 protease and phosphatase inhibitors (Thermo Fisher), reduced with 5 mM dithiothreitol, alkylated with 10 mM
511 iodoacetamide, and digested overnight with trypsin. Peptides were labeled using the TMTpro 16-plex kit
512 (Thermo Fisher Scientific), pooled, and fractionated by high-pH reversed-phase chromatography. Fractions
513 were analyzed on an Orbitrap Lumos mass spectrometer (Thermo Fisher Scientific) coupled to a 3000 RSLC
514 nano-UPLC system using a 26-min gradient on a 1.7 µm C18 column (Waters). MS scans were acquired at
515 120,000 resolution with a 3 s cycle time, and the top precursors (charge 2–5) were selected for MS/MS with
516 higher-energy collisional dissociation (HCD 35%), 50,000 resolution, 125k AGC target, and 86 ms maximum
517 injection time, with dynamic exclusion of 20 s. Raw files were processed in Proteome Discoverer v3.0 using
518 Sequest HT against the UniProt human proteome database for TMT-based quantification, and protein
519 abundances were normalized across channels for downstream analysis.
520
521 **Olink-based proteomics of cerebrospinal fluid**
522 Cerebrospinal fluid (CSF) samples (n=24; Extended Data Table 1) were analyzed using the Olink Explore 384
523 platform (Thermo Fisher Scientific). The following panels were included: Cardiometabolic, Cardiometabolic II,
524 Inflammation, Inflammation II, Neurology, Neurology II, Oncology, and Oncology II. Data processing, QC,
525 and normalization were performed using the Explore Calculation Module v3.8.1, applying intensity
526 normalization on a $\log_2$ scale.
527
528 **snRNA-seq**
529 We ran bcl2fastq, followed by CellRanger v7.0.1 to generate RNA, ATAC, and hash count matrices using the
530 GRCh38 genome. Downstream analyses were conducted in R Seurat v4.2.0 package[33]. RNA and ATAC count
531 matrices were treated separately to retain nuclei with sufficient modality-specific quality. For snRNA-seq we
532 excluded droplets with >12,000 or <500 features and <500 counts. Ambient RNA contamination was corrected

533 using SoupX v1.6.2[34] with autoEstCont (tfidMin=0.7–0.9) to ensure at least 100 genes were used for estimation.
534 Nuclei were demultiplexed using HTOdemux, which also flagged hash doublets.
535
536 In alignment with previously established strategies for guided doublet removal[35,36] we leveraged previously
537 reported markers for the choroid plexus, brain vasculature, and brain immune cells in mouse and human (see
538 Extended Data Table 30). Data were normalized and scaled incorporating the top 3k variable features and
539 reported markers, which were then used for Principal Component Analysis (PCA, top 30 embeddings),
540 Harmony[37] v0.1.0 integration by sequencing library, dimensionality reduction (UMAP), and clustering
541 (Louvain algorithm, res=0.03-0.7)[38]. Positive marker genes were identified using a bimodal Wilcox rank sum-
542 test ($\log_2$FC>0.25, p<0.05). Since 'dark' epithelial cells are characterized by high mitochondrial content[39,40],
543 mitochondrial content >5% were only retained in the epithelial cluster. Nuclei with mixed cluster signatures
544 were excluded, known doublets were removed and misclustered cells were removed from UMAP plots. Data
545 were iteratively reprocessed as above but in an unsupervised manner with the top 3k unknown variable features
546 to identify major and sub cell types.
547
548 **snATAC-seq**
549 Following the generation of raw count matrices, we utilized Seurat v4.2.0[33] and Signac 1.10.0[41] . Low-quality
550 droplets with total fragments <100 or >5,000, blacklist ratio >0.1, nucleosome signal >4, and transcription start
551 site (TSS) enrichment score <3 was excluded. After demultiplexing with HTODemux, doublets were removed
552 using the semi-supervised method described above (Methods: snRNA-seq). Chromatin accessibility data were
553 normalized using RunTFIDF, reduced with RunSVD, and the top 30 components were used for dimensionality
554 reduction and clustering. To annotate clusters, we generated a pseudo-expression "activity" matrix, which was
555 normalized, scaled and a bimodal Wilcoxon rank-sum test ($\log_2$FC > 0.25, p<0.05) was used to identify cell
556 type markers. We annotated chromatin features with the UCSC Genome Browser, motif analysis with
557 motifmatchR v1.31.1[42] (JASPAR 2022, default thresholds), and transcription factor activity with Signac
558 Footprint (default settings).
559
560 **Spatial transcriptomics**
561 Initial preprocessing followed the AtoMx pipeline (MAN-10162-03; software v1.2). Cellpose v2 was used for
562 segmentation (non-neuro human tissue, cell dilation: 2.17 µm, cell diameter: 7.28 µm, nucleus size: 7.2 µm,
563 membrane size: 5.7µm, Models: cyto2, flow threshold: 0.1, probability threshold: 2, min. size: 3.6µm) followed
564 by QC and flat file export to Seurat v5.1.0[43]. Segmented cells with <100 counts, >3500 counts, <50
565 features, >2000 features, qcCellsFlagged==T, or an area <10µm^2 were excluded. We used SCTransform
566 v.0.4.1[44,45]to correct, scale, and normalize; and harmony to correct for individual and slide effects. The semi-
567 supervised method described above (Methods: snRNA-seq) was used to identify potential segmentation errors

568 (e.g. cells with high expression of marker genes from multiple major cell types). These were excluded for
569 downstream cell type annotation (unsupervised, top 2k) and AD-differential testing but retained for spatial
570 neighborhood and CellChat analysis. Due to limitations of unsupervised clustering algorithms in resolving rare
571 cell types (<6,000 cells per major cell type), we applied a supervised mapping approach using the snRNA-seq
572 dataset as reference. Specifically, spatial transcriptomics data were annotated using RCTD[23] with default
573 parameters, leveraging pseudobulked snRNA-seq expression profiles for each major cell type as reference.
574

575 **Differential expression analyses**

576 We performed differential gene expression, protein abundance, and chromatin accessibility analyses using a
577 linear modeling framework with empirical Bayes moderation as implemented in voom and limma v3.54[46].
578 Where applicable, models were adjusted for age, sex, postmortem interval (PMI), and sequencing library. Genes
579 and proteins with fewer than two counts per sample or expressed in fewer than 1% of cells were excluded.
580 Accessible chromatin regions and gene activity scores with variance-standardized transformation (vst) scores
581 below 1 were removed. For the snRNA-seq dataset, samples with >100,000 total pseudobulked counts were
582 split by sequencing library to create technical replicates; samples with <60,000 counts were excluded. Genes
583 with a false discovery rate (FDR) <0.01 and absolute log2 fold change (LFC) >0.5 were considered
584 differentially expressed. For smaller datasets (spatial transcriptomics, chromatin accessibility (snATAC-seq),
585 and proteomics) validation thresholds were relaxed ($p < 0.05$, LFC > 0.2). We tested cell type specific
586 transcriptional signatures and correlated these between modalities. We tested contrasts between clinical
587 diagnostic (cogdx), neuropathological categories (adnc_ad), and cognitive decline (last cognitive score before
588 death) among major and minor cell types.
589

590 **Enrichment analysis**

591 Ranked gene lists were stratified by directionality and tested using fgsea v1.25[47] against Gene Ontology (GO)
592 Biological Process, Molecular Function, and Cellular Component pathways. A normalized enrichment score
593 (NES) >0.6 and FDR <0.15 for spatial transcriptomics, snATAC-seq, and proteomics were used to define
594 significant pathways. Enrichment and differential expression results were visualized using ClueGO v2.5.10[48],
595 Cytoscape v3.10.2, ComplexHeatmap[49,50], Seurat, and ggplot2 v3.4.4[51].
596

597 **Proportion analysis**

598 As previously described[52], we applied a linear modeling with empirical Bayes moderation to assess cell type
599 proportions as a function of cognitive diagnosis (cogdx). Where applicable, models were adjusted for
600 parenchymal contamination, age, sex, and PMI. Statistical significance was defined as FDR < 0.01.
601

602 **Pattern matching in snRNA-seq**

603 We applied a template matching algorithm[22] to identify genes associated with disease progression along three
604 possible positive and negative trajectories. Differentially expressed genes ($p<0.05$, LFC>0.25) from the MCI vs.
605 NCI, ADd vs. MCI, and ADd vs. NCI contrasts were classified as early-stage (significant in MCI vs. NCI and
606 ADd vs. MCI, but not AD vs. NCI), late-stage (significant in ADd vs. MCI and ADd vs. NCI, but not MCI vs.
607 NCI), and progressive (significant in MCI vs. NCI and ADd vs. NCI) patterns. Genes were correlated with the
608 corresponding stage template, and only those with $p < 0.05$ were retained.
609
610 **Nearest Neighbor analysis**
611 To obtain a better understanding of cell-cell interaction we included cells with mixed signatures and mapped
612 cells to their closest major cell type (Methods: Spatial transcriptomics data processing), only excluding cells
613 that did not meet QC metrics, parenchymal cells and red blood cells. This resulted in 166,607 total cells for
614 analysis. A spatial neighborhood matrix was generated using CellularNeighborhoods v0.0.0.9000 available
615 here: https://github.com/Nanostring-Biostats/CosMx-Analysis-Scratch-Space/tree/Main/_code/cellular-
616 neighborhoods. Each cell's neighborhood expression was calculated as the mean expression of a random 10-cell
617 subset of its 25 nearest neighbors, based on cell centroid x-y coordinates. We performed normalization/scaling,
618 PCA (50 components), Harmony (50 components, accounting for slide batch, individual, and AD status),
619 UMAP, and clustering (kmeans = 3) to obtain 3 spatial neighborhoods or 'niches'.
620
621 **CellChat**
622 We used CellChat v1.6.1[24] to infer intercellular communication networks among major cell types stratified per
623 cognitive diagnosis (MCI, MCI, and ADd) with default parameters for the snRNA-seq dataset and for spatial
624 transcriptomics after nearest neighbor analysis. For spatial transcriptomics, CellChat was run separately for
625 each niche with SCTransformed counts, computeCommunProb with a contact.range=20 microns,
626 interaction.range=250 microns, scale.distance=0.69 (empirically determined), and all other parameters default.
627 We also normalized cellchat metrics (interaction weight, net$prob, netP$prob, and centrality score) by the
628 number of cell pairs with the potential for interaction (e.g. within 250 microns), thereby accounting for
629 differences in cell number and density between NCI and AD, as well as across niches.
630
631 To identify disease-associated signaling pathways, objects for each cognitive diagnosis were merged and
632 comparative network analyses performed. A customrankNet() function was implemented to rank pathways with
633 $p<0.05$ by summed communication probability (weight) per condition, calculating relative contributions across
634 diagnostic groups. Pathway-level metrics (information flow and interaction counts) were extracted from the
635 netP slot of the merged object. To assess cell-type-specific signaling changes, centrality scores (incoming +
636 outgoing) were computed for each cell type and condition using netAnalysis_computeCentrality(). To ensure
637 robust conclusions, previously identified (Methods: Differential analyses: Expression) statistics for each ligand-

638 receptor pair were utilized and the average log_2FC of ligand and receptor(s) was calculated. We removed non-
639 directional or low-confidence interactions (ligand-receptor pairs with absolute combined $log_2FC < 0.05$, ligand
640 detected in < 5% of sender cells, receptor detected in < 5% of receiver cells, and/or net$p > 0.05). At the
641 pathway level, median log_2FC was calculated per pathway and a Wilcoxon signed-ranked test was applied to
642 pathways with ≥ 3 interactions followed by FDR correction. Pathways defined as significant had absolute
643 median $log_2FC \geq 0.15$, FDR ≤ 0.01, absolute AD-differential net centrality > 0.0001, and matched centrality and
644 median log_2FC directionality.
645
646 **Cell-cell distance-based analysis**
647 We converted centroid x-y coordinates from pixels to microns (x0.18) and computed per-cell distances to the
648 nearest cell type (e.g. Mural/Endothelial, Epithelial, Parenchymal), then calculated and plotted per-individual
649 averages across spatial niches or cell subtypes. We performed a Kruskal-Wallis test and used Dunn's test with
650 Benjamini-Hochberg correction for multiple testing.
651
652 **Immunohistochemistry**
653 Human FFPE CP sections were stained using a Bond-Rx research stainer (Leica Biosystems). Briefly, slides
654 were baked for 60 min at 60°C prior to dewaxing for 30 s at 72°C. For multiplexed cell typing, an Opal 6-plex
655 detection kit (Akoya Biosciences #NEL871001KT) was used as follows; slides were incubated with CD45
656 (1:50) for 30 min followed by 10 min Opal polymer HRP Ms+Rb and 10 min Opal signal development with
657 Opal 620 diluted at 1:150. Slides were antigen retrieved for 20 min in pH 6.0 citrate buffer solution (Leica
658 Biosystems #AR9961) and the process was repeated with DCN (1:100; Opal 570 (1:150)), TTR (1:500; Opal
659 690 (1:150)), PECAM (1:50; Opal 520 (1:150)) and ACTA2 (1:1000; Opal 480 (1:150)). For ciliary rootlet
660 structures, slides were subjected to HIER with a pH 9.0 EDTA buffer solution (Leica Biosystems #AR9640) for
661 20 min at 100°C followed by 10 min peroxide block. CROCC (1:100) and TTR (1:500) were incubated together
662 for 60 minutes followed by 60 min of secondary anti-rabbit Alexa Fluor 647 (1:1000) for CROCC. The TTR
663 antibody was detected with a Mouse IgG-HRP secondary, incubated for 60 min, followed by a 5 min incubation
664 with TSA Fluorescein. All slides were then incubated with Trueblack quencher for 1 minute, counter stained
665 with spectral DAPI for 5 min, and mounted. Imaging was performed using a PhenoImager (Akoya Biosciences)
666 at 40X. ROIs were selected using Phenochart 2.2.0 (Akoya Biosciences) and spectrally unmixed composite
667 TIFs were generated using inForm (Akoya Biosciences).
668
669 For CROCC puncta analysis, images were imported into ImageJ and split into individual channels. CROCC
670 channel image was converted into 8-bit and threshold was set to mask only the puncta. Analyze particles tool in
671 ImageJ was run with the following parameters: Size=1.5-25.0 µm and Circularity= 0.1-1.0. The results were
672 exported and analyzed in GraphPad prism (v10.5.0). For classification of TTR+ epithelial cells, the raw

673 composite TIFs were analyzed using Qupath (v0.5). Cells were defined in each ROI using QuPath Cell
674 Detection tool with the following parameters, requested pixel size = 0.5µm, background radius = 8µm, median
675 filter radius =0µm, Sigma value for Gaussian filter = 1.5µm, minimum nucleus area = 10µm^2, maximum
676 nucleus area =400µm^2, and intensity threshold = 2. Cell parameters include a cell expansion of 5µm from the
677 cell nucleus, and general parameters include smoothing of the detected nucleus/cell boundaries. Shape, intensity
678 and smoothing features were added for all detections, and the "Train object classifier" tool was used to classify
679 the TTR+ epithelial cells. All measurements were exported and analyzed in GraphPad prism (v10.5.0).
680

681 **Multiplex immunohistochemical staining using Akoya Phenocycler fusion (PCF)**

682 Human FFPE CP sections were stained using the Akoya Biosciences Phenocycler Fusion 2.0 workflow as per
683 manufacturer's instructions. Briefly, the slides were baked overnight at 60 degrees and de-waxed, hydrated and
684 antigen retrieval performed in a pressure cooker for 20 min in AR9 buffer. Staining was performed for 3 hrs at
685 room temperature followed by washing and post-fixation steps. Imaging was performed on Akoya Phenocycler
686 Fusion 2.0 instrument at 20X. Qptiff image files generated were imported into QuPath (v0.5) for quantitative
687 analysis.
688

689 **Phenocycler Fusion Image Analysis**

690 For analysis of CD163+ BAM cells, ROIs were defined in each image and QuPath Cell Detection tool was used
691 with following parameters: detection channel= CD163, requested pixel size = 0.5µm, background radius =
692 20µm, median filter radius =0µm, Sigma value for Gaussian filter = 1.5µm, minimum nucleus area = 15µm^2,
693 maximum nucleus area =400µm^2, and intensity threshold = 50. No cell parameters were selected, and general
694 parameters include smoothing of the detected nucleus/cell boundaries. HLA-DR and CD68 intensity
695 measurements from CD163$^+$ cells were exported and analyzed in GraphPad Prism (v10.5.0).
696

697 For T-cell analysis, ROIs were defined in each image and QuPath Cell Detection tool was used with following
698 parameters: detection channel= CD3e, requested pixel size = 0.5µm, background radius = 20µm, median filter
699 radius =0µm, Sigma value for Gaussian filter = 1.5µm, minimum nucleus area = 10µm^2, maximum nucleus area
700 =400µm^2, and intensity threshold = 50. No cell parameters were selected, and general parameters include
701 smoothing of the detected nucleus/cell boundaries. Shape, intensity and smoothing features were added for all
702 detections, and the "Train object classifier" tool was used to classify the CD4+ and CD8+ T-cells. All T-cells
703 were manually annotated based on whether they are present inside (non-infiltrating) or outside (infiltrating) of
704 Caveolin/Collagen IV+ vessels. The numbers of infiltrated T cells were plotted relative to the area of the ROIs
705 and analyzed in GraphPad Prism (v10.5.0).
706

707 **Movat's Pentachrome staining and analysis**

Human FFPE CP sections were stained with Movat's Pentachrome stain kit (Abcam, ab245884) as per the manufacturer's instructions in two batches. Slides were imaged using the Phenocycler Imaging system (Akoya Biosciences) at 40X. 4-10 ROIs (928µm x 697µm) were selected from each case using Akoya Phenochart 2.2.0 and RGB TIFs were exported using inForm (Akoya Biosciences).

Images were processed using the Colour Deconvolution Package (https://blog.bham.ac.uk/intellimic/g-landini-software/colour-deconvolution-2/) in ImageJ (v1.54) to extract the yellow channel. Images were converted to 8 bit and exported as image txt files for further processing in R. Background subtraction was performed to align batches, and pixels that did not correspond to tissue were excluded. For each ROI, the distribution of pixel intensities was calculated. The pixel distributions for each individual were averaged to present the distribution for each disease group, plotted with ggplot2. The AUC for each ROI at high collagen (cutoff of 200) was calculated using the trapz() function from the pracma library (v2.4.4) and a one-way ANOVA performed to test significance.

References

1. Saunders, N. R., Dziegielewska, K. M., Fame, R. M., Lehtinen, M. K. & Liddelow, S. A. The choroid plexus: a missing link in our understanding of brain development and function. *Physiol. Rev.* **103**, 919–956 (2023).
2. Verhaege, D. *et al.* Newly discovered base barrier cells provide compartmentalization of choroid plexus, brain and CSF. *bioRxiv* (2024) doi:10.1101/2024.07.08.601696.
3. Gião, T., Teixeira, T., Almeida, M. R. & Cardoso, I. Choroid plexus in Alzheimer's disease-the current state of knowledge. *Biomedicines* **10**, 224 (2022).
4. Rasmussen, M. K., Mestre, H. & Nedergaard, M. Fluid transport in the brain. *Physiol. Rev.* **102**, 1025–1151 (2022).
5. Attier-Zmudka, J. *et al.* Decreased cerebrospinal fluid flow is associated with cognitive deficit in elderly patients. *Front. Aging Neurosci.* **11**, 87 (2019).
6. Ferdinando, H., Moradi, S., Korhonen, V., Kiviniemi, V. & Myllylä, T. Altered cerebrovascular-CSF coupling in Alzheimer's Disease measured by functional near-infrared spectroscopy. *Sci. Rep.* **13**, 22364 (2023).
7. Xu, H. *et al.* The choroid plexus synergizes with immune cells during neuroinflammation. *Cell* **187**, 4946-4963.e17 (2024).
8. Pichet Binette, A. *et al.* Proteomic changes in Alzheimer's disease associated with progressive Aβ plaque and tau tangle pathologies. *Nat. Neurosci.* **27**, 1880–1891 (2024).
9. Shen, Y. *et al.* Systematic proteomics in Autosomal dominant Alzheimer's disease reveals decades-early changes of CSF proteins in neuronal death, and immune pathways. *medRxiv* (2024) doi:10.1101/2024.01.12.24301242.
10. Liu, R. *et al.* Choroid plexus epithelium and its role in neurological diseases. *Front. Mol. Neurosci.* **15**, 949231 (2022).
11. Stopa, E. G. *et al.* Comparative transcriptomics of choroid plexus in Alzheimer's disease, frontotemporal dementia and Huntington's disease: implications for CSF homeostasis. *Fluids Barriers CNS* **15**, 18 (2018).
12. Delvenne, A. *et al.* Involvement of the choroid plexus in Alzheimer's disease pathophysiology: findings from mouse and human proteomic studies. *Fluids Barriers CNS* **21**, 58 (2024).
13. Brkic, M. *et al.* Neurobiology of Disease. *J. Neurosci.* **35**, 12766–12778 (2015).
14. Yan, Z.-J., Ye, M., Li, J., Zhang, D.-F. & Yao, Y.-G. Early transcriptional and cellular abnormalities in choroid plexus of a mouse model of Alzheimer's disease. *Mol. Neurodegener.* **20**, 62 (2025).
15. Tijms, B. M. *et al.* Cerebrospinal fluid proteomics in patients with Alzheimer's disease reveals five molecular subtypes with distinct genetic risk profiles. *Nat. Aging* **4**, 33–47 (2024).
16. Bennett, D. A. *et al.* Religious Orders Study and Rush Memory and Aging Project. *J. Alzheimers. Dis.* **64**, S161–S189 (2018).

758 17. Kearns, N. A. *et al.* Dissecting the human leptomeninges at single-cell resolution. *Nat. Commun.* **14**, 7036
759 (2023).
760 18. Fullard, J. F. *et al.* Single-nucleus transcriptome analysis of human brain immune response in patients with
761 severe COVID-19. *Genome Med.* **13**, 118 (2021).
762 19. Yang, A. C. *et al.* Dysregulation of brain and choroid plexus cell types in severe COVID-19. *Nature* **595**,
763 565–571 (2021).
764 20. Sérot, J., Béné, M., Foliguet, B. & Faure, G. Morphological alterations of the choroid plexus in late-onset
765 Alzheimer's disease. *Acta Neuropathol.* **99**, 105–108 (2000).
766 21. Pavlidis, P. & Noble, W. S. Analysis of strain and regional variation in gene expression in mouse brain.
767 *Genome Biol.* **2**, RESEARCH0042 (2001).
768 22. Cable, D. M. *et al.* Robust decomposition of cell type mixtures in spatial transcriptomics. *Nat. Biotechnol.*
769 **40**, 517–526 (2022).
770 23. Jin, S. *et al.* Inference and analysis of cell-cell communication using CellChat. *Nat. Commun.* **12**, 1088
771 (2021).
772 24. Kunis, G. *et al.* IFN-γ-dependent activation of the brain's choroid plexus for CNS immune surveillance
773 and repair. *Brain* **136**, 3427–3440 (2013).
774 25. Reboldi, A. *et al.* C-C chemokine receptor 6-regulated entry of TH-17 cells into the CNS through the
775 choroid plexus is required for the initiation of EAE. *Nat. Immunol.* **10**, 514–523 (2009).
776 26. Fernández-Klett, F. & Priller, J. The fibrotic scar in neurological disorders. *Brain Pathol.* **24**, 404–413
777 (2014).
778 27. Xue, X. *et al.* Heterogeneous fibroblasts contribute to fibrotic scar formation after spinal cord injury in
779 mice and monkeys. *Nat. Commun.* **15**, 6321 (2024).
780 28. Dias, D. O. *et al.* Pericyte-derived fibrotic scarring is conserved across diverse central nervous system
781 lesions. *Nat. Commun.* **12**, 5501 (2021).
782 29. Bennett, D. A. *et al.* Neuropathology of older persons without cognitive impairment from two community-
783 based studies. *Neurology* **66**, 1837–1844 (2006).
784 30. Schneider, J. A., Arvanitakis, Z., Leurgans, S. E. & Bennett, D. A. The neuropathology of probable
785 Alzheimer disease and mild cognitive impairment. *Ann. Neurol.* **66**, 200–208 (2009).
786 31. Arvanitakis, Z. *et al.* Cerebral amyloid angiopathy pathology and cognitive domains in older persons. *Ann.*
787 *Neurol.* **69**, 320–327 (2011).
788 32. McGinnis, C. S. *et al.* MULTI-seq: sample multiplexing for single-cell RNA sequencing using lipid-tagged
789 indices. *Nat. Methods* **16**, 619–626 (2019).
790 33. Hao, Y. *et al.* Integrated analysis of multimodal single-cell data. *Cell* **184**, 3573-3587.e29 (2021).
791 34. Young, M. D. & Behjati, S. SoupX removes ambient RNA contamination from droplet-based single-cell
792 RNA sequencing data. *Gigascience* **9**, (2020).

35. Green, G. S. *et al.* Cellular communities reveal trajectories of brain ageing and Alzheimer's disease. *Nature* **633**, 634–645 (2024).
36. Dani, N. *et al.* A cellular and spatial map of the choroid plexus across brain ventricles and ages. *Cell* **184**, 3056-3074.e21 (2021).
37. Korsunsky, I. *et al.* Fast, sensitive and accurate integration of single-cell data with Harmony. *Nat. Methods* **16**, 1289–1296 (2019).
38. Waltman, L. & van Eck, N. J. A smart local moving algorithm for large-scale modularity-based community detection. *Eur. Phys. J. B* **86**, 6–471 (2013).
39. Garma-Aviña, A. Cytology of the normal and abnormal choroid plexi in selected domestic mammals, wildlife species, and man. *J. Vet. Diagn. Invest.* **16**, 283–292 (2004).
40. Pellegrini, L. *et al.* Human CNS barrier-forming organoids with cerebrospinal fluid production. *Science* **369**, eaaz5626 (2020).
41. Stuart, T., Srivastava, A., Madad, S., Lareau, C. A. & Satija, R. Single-cell chromatin state analysis with Signac. *Nat. Methods* **18**, 1333–1341 (2021).
42. Schep, A. *Fast Motif Matching in R*. https://bioconductor.org/packages/devel/bioc/manuals/motifmatchr/man/motifmatchr.pdf (2025).
43. Hao, Y. *et al.* Dictionary learning for integrative, multimodal and scalable single-cell analysis. *Nat. Biotechnol.* **42**, 293–304 (2024).
44. Choudhary, S. & Satija, R. Comparison and evaluation of statistical error models for scRNA-seq. *Genome Biol.* **23**, 27 (2022).
45. Hafemeister, C. & Satija, R. Normalization and variance stabilization of single-cell RNA-seq data using regularized negative binomial regression. *Genome Biol.* **20**, 296 (2019).
46. Ritchie, M. E. *et al.* limma powers differential expression analyses for RNA-sequencing and microarray studies. *Nucleic Acids Res.* **43**, e47 (2015).
47. Korotkevich, G., Sukhov, V. & Sergushichev, A. Fast gene set enrichment analysis. *bioRxiv* (2016) doi:10.1101/060012.
48. Bindea, G. *et al.* ClueGO: a Cytoscape plug-in to decipher functionally grouped gene ontology and pathway annotation networks. *Bioinformatics* **25**, 1091–1093 (2009).
49. Gu, Z., Eils, R. & Schlesner, M. Complex heatmaps reveal patterns and correlations in multidimensional genomic data. *Bioinformatics* **32**, 2847–2849 (2016).
50. Gu, Z. Complex heatmap visualization. *Imeta* **1**, e43 (2022).
51. Wickham, H. *Ggplot2: Elegant Graphics for Data Analysis*. (Springer International Publishing, Cham, Switzerland, 2016).
52. Phipson, B. *et al.* propeller: testing for differences in cell type proportions in single cell data. *Bioinformatics* **38**, 4720–4726 (2022).

Main Figures

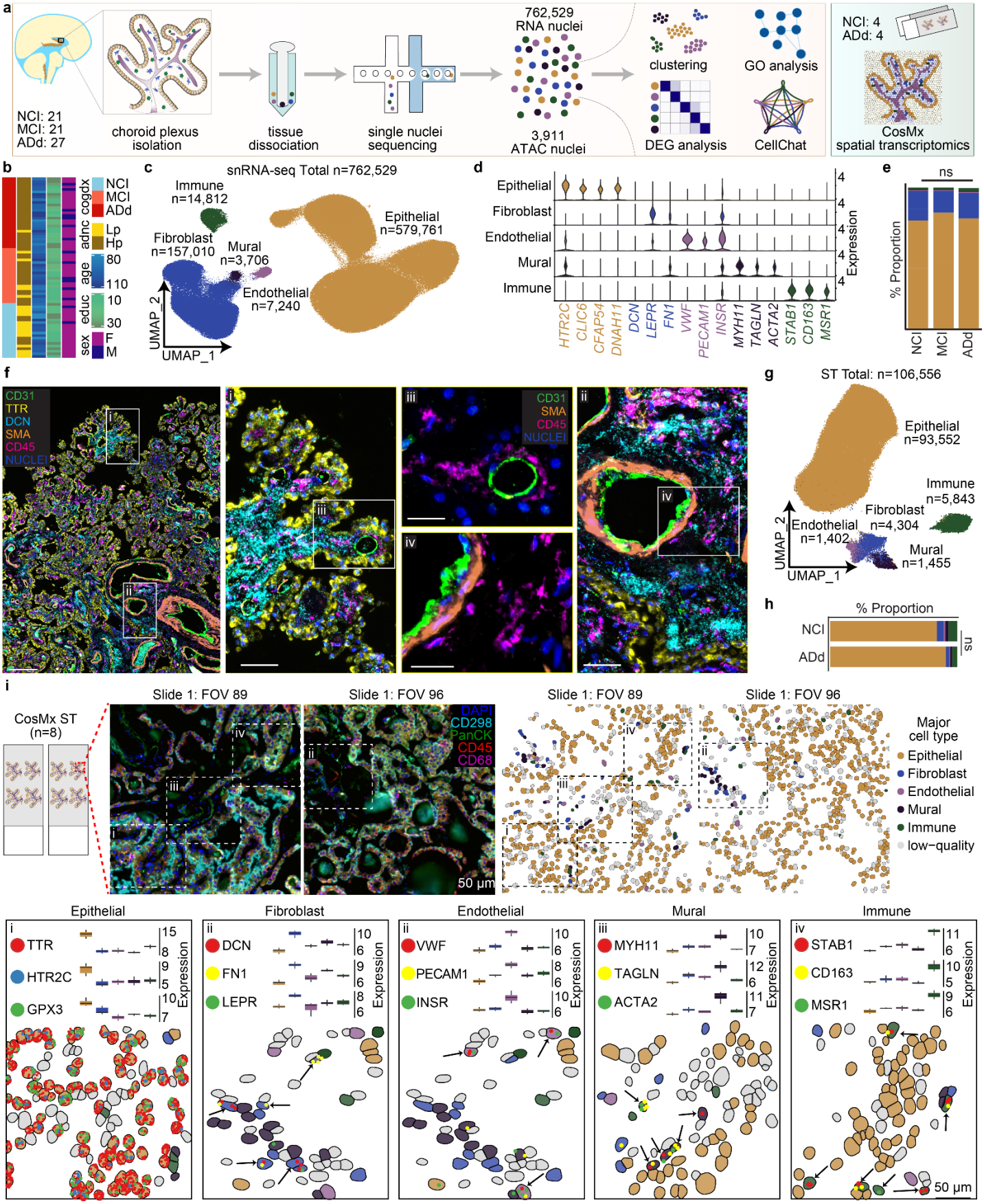

Fig. 1: Major cell classes of the human choroid plexus

a, Study design overview. snRNA-seq was performed on 69 participants (762,529 nuclei) and snATAC-seq was performed on nuclei from 6 participants (3,238 nuclei), and spatial transcriptomics (ST) on 8 participants (106,556 segmented cells).

b, Participant demographics, balanced for age, sex, and education (educ). Clinical (cogdx) and neuropathological (ad_adnc) diagnoses are indicated. See Extended Data Table 1.

c, snRNA-seq UMAP colored by major cell types.

d, snRNA-seq canonical marker expression violin plot per cell cluster (pseudobulk FDR < 0.01, $\log_2$FC > 0.25). See Extended Data Table 2.

e, snRNA-seq major cell type proportions stratified by clinical diagnosis (all not significant, FDR > 0.01, ns).

f, Multiplexed immunohistochemistry staining for CD31, TTR, DCN, SMA, CD45 and DAPI. Scale bars = 200 µm (overview), 50 µm (i, ii) and 20 µm (iii, iv).

g, Unsupervised spatial transcriptomics (ST) UMAP projection of major cell types.

h, Proportion of epithelial subclusters in ST data.

i, Adjacent spatial transcriptomics fields of view (FOVs #1.89 and #1.96) Upper left: immunostaining. Upper right: segmented cells colored by major cell type. Below: transcript localization with quantified pseudobulk expression ($\log_2$counts; upper) and example FOV (lower). Arrows indicate marker localization. Scale bars, 50 µm.

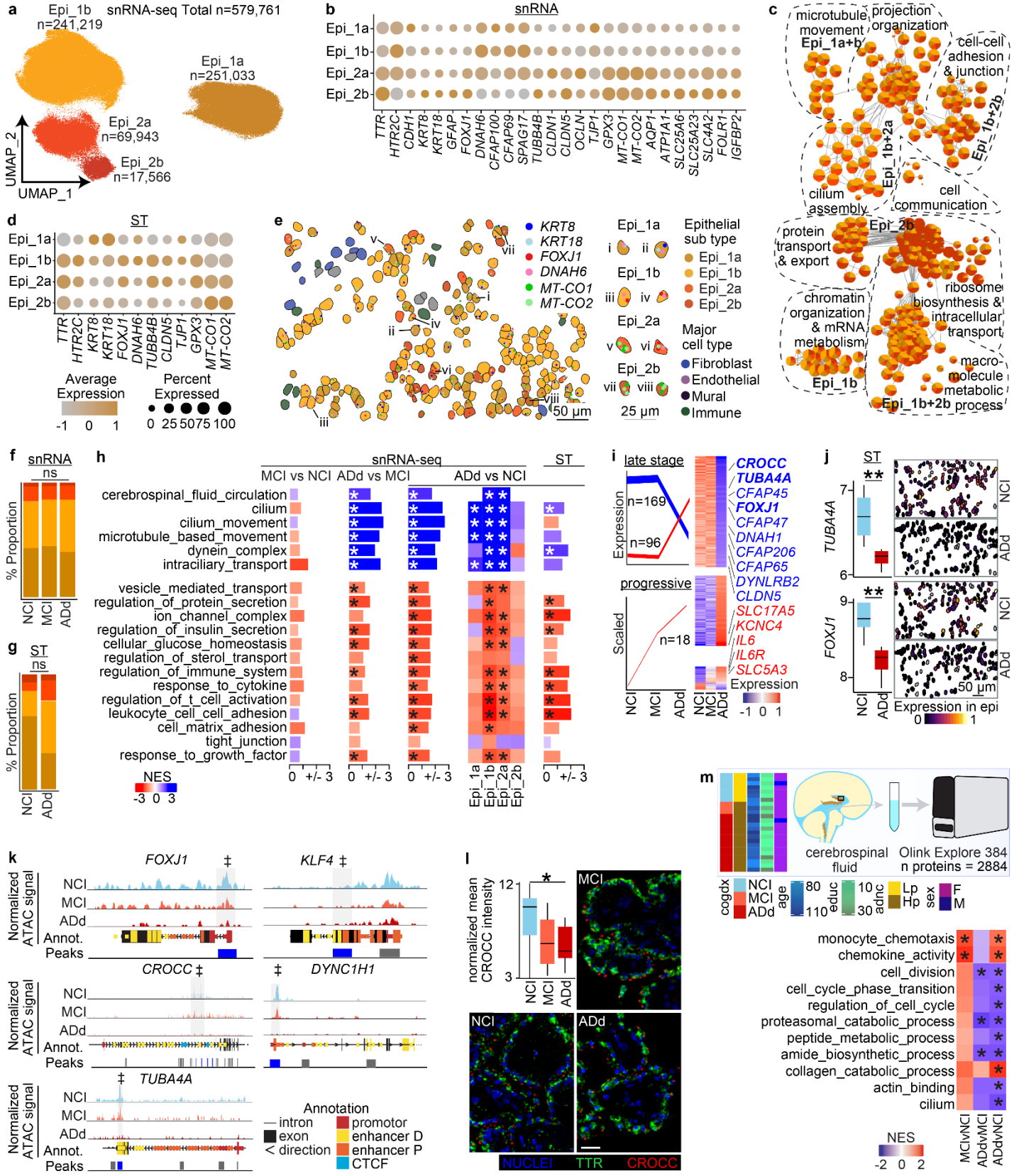
a
snRNA-seq Total n=579,761
Epi_1b n=241,219
Epi_1a n=251,033
Epi_2a n=69,943
Epi_2b n=17,566
UMAP_2
UMAP_1
b
snRNA
Epi_1a
Epi_1b
Epi_2a
Epi_2b
TTR HTR2C CDH1 KRT8 KRT18 GFAP FOXJ1 DNAH6 CFAP100 CFAP69 SPAG17 TUBB4B CLDN1 CLDN5 OCLN TJP1 GPX3 MT-CO1 MT-CO2 AQP1 ATP1A1 SLC25A6 SLC25A23 SLC4A2 FOLR1 IGFBP2
c
microtubule movement
projection organization
Epi_1a+b
cell-cell adhesion & junction
Epi_1b+2a
Epi_1b+2b
cilium assembly
cell communication
protein transport & export
Epi_2b
chromatin organization & mRNA metabolism
ribosome biosynthesis & intracellular transport
Epi_1b
macro-molecule metabolic process
Epi_1b+2b
d
ST
Epi_1a
Epi_1b
Epi_2a
Epi_2b
TTR HTR2C KRT8 KRT18 FOXJ1 DNAH6 TUBB4B CLDN5 TJP1 GPX3 MT-CO1 MT-CO2
Average Expression
-1 0 1
Percent Expressed
0 25 50 75 100
e
KRT8
KRT18
FOXJ1
DNAH6
MT-CO1
MT-CO2
50 µm
Epi_1a
Epi_1b
Epi_2a
Epi_2b
25 µm
Epithelial sub type
Epi_1a
Epi_1b
Epi_2a
Epi_2b
Major cell type
Fibroblast
Endothelial
Mural
Immune
f
snRNA
ns
% Proportion
NCI MCI ADd
g
ST
ns
% Proportion
NCI ADd
h
snRNA-seq
MCI vs NCI
ADd vs MCI
ADd vs NCI
ST
cerebrospinal_fluid_circulation
cilium
cilium_movement
microtubule_based_movement
dynein_complex
intraciliary_transport
vesicle_mediated_transport
regulation_of_protein_secretion
ion_channel_complex
regulation_of_insulin_secretion
cellular_glucose_homeostasis
regulation_of_sterol_transport
regulation_of_immune_system
response_to_cytokine
regulation_of_t_cell_activation
leukocyte_cell_cell_adhesion
cell_matrix_adhesion
tight_junction
response_to_growth_factor
NES
-3 0 3
0 +/- 3
Epi_1a Epi_1b Epi_2a Epi_2b
i
late stage
Expression
n=169
n=96
progressive
Scaled
n=18
NCI MCI ADd
CROCC
TUBA4A
CFAP45
FOXJ1
CFAP47
DNAH1
CFAP206
CFAP65
DYNLRB2
CLDN5
SLC17A5
KCNC4
IL6
IL6R
SLC5A3
Expression
-1 0 1
j
ST
TUBA4A
FOXJ1
NCI
ADd
50 µm
Expression in epi
0 1
k
FOXJ1
KLF4
CROCC
DYNC1H1
TUBA4A
Normalized ATAC signal
NCI
MCI
ADd
Annot.
Peaks
Annotation
intron
exon
< direction
promotor
enhancer D
enhancer P
CTCF
l
normalized mean CROCC intensity
12
3
NCI MCI ADd
NUCLEI TTR CROCC
m
cerebrospinal fluid
Olink Explore 384
n proteins = 2884
cogdx
NCI
MCI
ADd
age
80
110
educ
10
30
adnc
Lp
Hp
sex
F
M
monocyte_chemotaxis
chemokine_activity
cell_division
cell_cycle_phase_transition
regulation_of_cell_cycle
proteasomal_catabolic_process
peptide_metabolic_process
amide_biosynthetic_process
collagen_catabolic_process
actin_binding
cilium
MCIvNCI
ADdvMCI
ADdvNCI
NES
-2 0 2

Fig. 2: Progressive epithelial inflammation and late ciliary loss in Alzheimer's disease

a, snRNA-seq UMAP projection colored by epithelial subtypes.

b, Epithelial subtype-defining marker dot plot (FDR < 0.01, $\log_2$FC > 0.25). See Extended Data Table 7.

c, Epithelial subtype GO enrichment network plot (ClueGO on subtype-defining markers) grouped by functional category.

d, Unsupervised spatial transcriptomics (ST) confirmation of epithelial subtype-defining marker dot plot. See Extended Data Table 8.

e, Spatial localization of epithelial subtypes overlaid with subtype-defining transcript localization; FOV: 1.186. Scale bar: 50µm. Right: Selected examples. Scale bar: 25 µm.

f-g, snRNA-seq (f) and spatial transcriptomics (g) epithelial subtype proportions across disease states. Linear mixed model on proportions (* FDR < 0.01).

h, Select GO pathways (via fgsea on ranked t statistics) of DEGs throughout clinical disease in snRNA-seq (SN) and matched spatial transcriptomics (ST) (*FDR < 0.15). See Extended Data Table 10-12.

i, Disease temporal dynamics of DEGs. "Late-stage specific" genes: ADd ≠ NCI & MCI; "progressive" genes: NCI ≠ MCI & ADd and MCI ≠ ADd. Left: line plots indicate the mean of scaled gene expression; line width corresponds to the number of genes following each trajectory. Right: heatmap per stage select genes representing key GO pathways are labelled (nominal p < 0.05, $\log_2$FC > ±0.25, trajectory correlation p < 0.05).

j, Spatial transcriptomics expression of select cilia genes (left: boxplots of pseudobulk expression ($\log_2$counts), median, interquartile range, min/max, ** FDR < 0.01; right: normalized expression in epithelial cells in example FOVs for NCI or ADd). Scale bars, 50 µm.

k, Differentially accessible chromatin peaks of select cilia genes throughout clinical disease progression (‡ nominal p<0.05 ADd vs NCI). Genome-specific annotations and accessible peaks are shown below. See Extended Data Table 13.

l, Mean CROCC intensity per TTR+ epithelial cell normalized to Hoechst intensity. Upper left: box plots throughout clinical disease progression (median, interquartile range, min/max; n = 9 NCI, 12 MCI, 9 ADd). One-way ANOVA $F(2,27) = 4.135$, $p<0.05$; Tukey's HSD * $p<0.05$. Right/lower: representative immunohistochemistry of DAPI, TTR and CROCC per group. Scale bar: 50 µm.

m, Selected GO pathways of CSF protein data throughout clinical disease progression (via fgsea on ranked t statistics; * FDR < 0.15). See Extended Data Table 14.

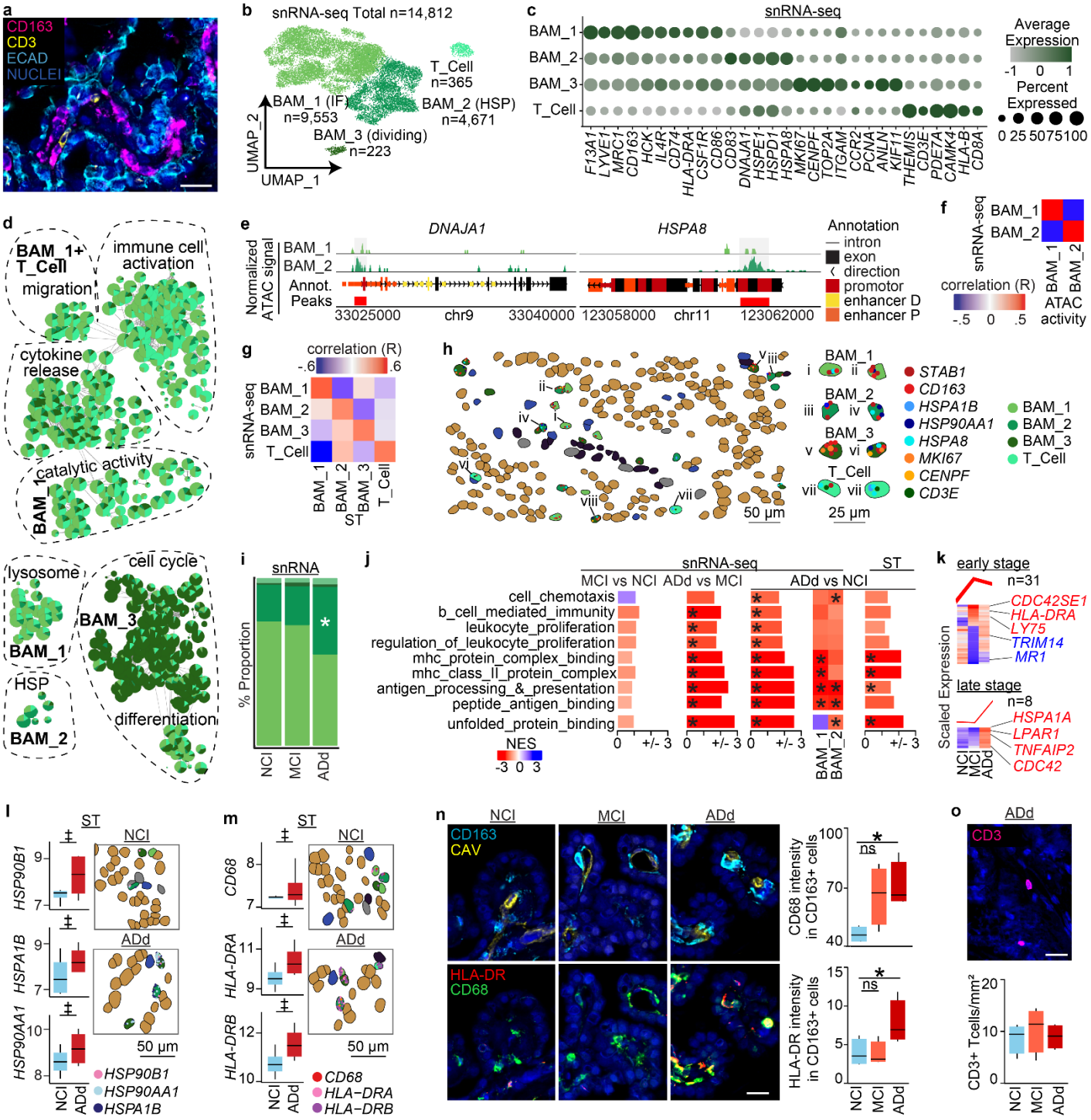

Fig. 3: Border-associated macrophages shifted from inflammatory to stress-associated states in Alzheimer's disease

a, Phenocycler fusion multiplexed immunostaining of DAPI, CD163, CD3 and E-cadherin (ECAD). Scale bar: 50µm.

b, snRNA-seq UMAP of immune cell subclusters.

c, Immune subtype defining marker dot plot (FDR < 0.01, $\log_2$ fold change > 0.25). See Table Extended Data Table 15.

d, Immune subtype GO enrichment network plot (ClueGo on subtype-defining markers) grouped by functional category and color-coded by immune subtype.

927 **e,** Differentially accessible chromatin peaks of select HSP genes per subtype. Genome-specific annotations and
928 accessible peaks are shown below.
929 **f,** Pearson correlation of chromatin accessibility (ATAC activity) and snRNA-seq expression among shared
930 immune substates.
931 **g,** Pearson correlation of supervised spatial transcriptomics (ST) and snRNA-seq expression among immune
932 substates.
933 **h,** Spatial localization of immune subtypes overlaid with subtype-defining marker expression; FOV: 1.186.
934 Scale bar: 50µm. Right: Selected examples. Scale bar: 25 µm.
935 **i,** Subtype proportions stratified by clinical diagnosis (* BAM_2 FDR < 0.01).
936 **j,** Select GO pathways (via fgsea on ranked t statistics) of DEGs throughout clinical disease in snRNA-seq and
937 matched spatial transcriptomics (*FDR < 0.15). See Extended Data Table 17-19.
938 **k,** Disease temporal dynamics of DEGs. "early stage" genes: NCI vs. MCI; "Late-stage specific" genes: ADd ≠
939 NCI & MCI. Upper: line plots indicate the mean of scaled gene expression; line width corresponds to the
940 number of genes following each trajectory. Lower: heatmap per stage; select genes representing key GO
941 pathways are labelled ($p < 0.05$, $\log_2 FC > \pm 0.25$, trajectory correlation $p < 0.05$).
942 **l-m,** Spatial transcriptomics gene expression of select HSP (**l**) and inflammation (**m**) Left: boxplots of
943 pseudobulk expression ($\log_2$counts) (median, interquartile range, min/max, ‡ nominal $p < 0.05$). Right: Spatial
944 localization of expression in NCI FOV #1.168 and AD FOV #2.24. Scale bar: 50 µm.
945 **n,** Left: Representative Phenocycler fusion immunofluorescence of HLA-DR and CD68, or CD163 and
946 caveolin (CAV) with DAPI for NCI and ADd. Scale bar: 50µm. Right: box plots of mean HLA-DR or CD68
947 intensity within CD163+ cells in NCI or ADd (median, interquartile range, and full range, $*p \leq 0.05$).
948 Welch's test HLA-DR: p=0.0582; CD68: p=0.01.
949 **o,** Representative Phenocycler fusion immunofluorescence of DAPI, CD3 and CD163. Scale bar, 50µm. Right:
950 Box plot of the numbers of CD4+ and CD8+ CD3+ T cells in NCI or ADd tissue (median, interquartile range,
951 and full range). Non-significant (ns).
952
953
954
955
956
957
958
959
960
961
962
963
964
965

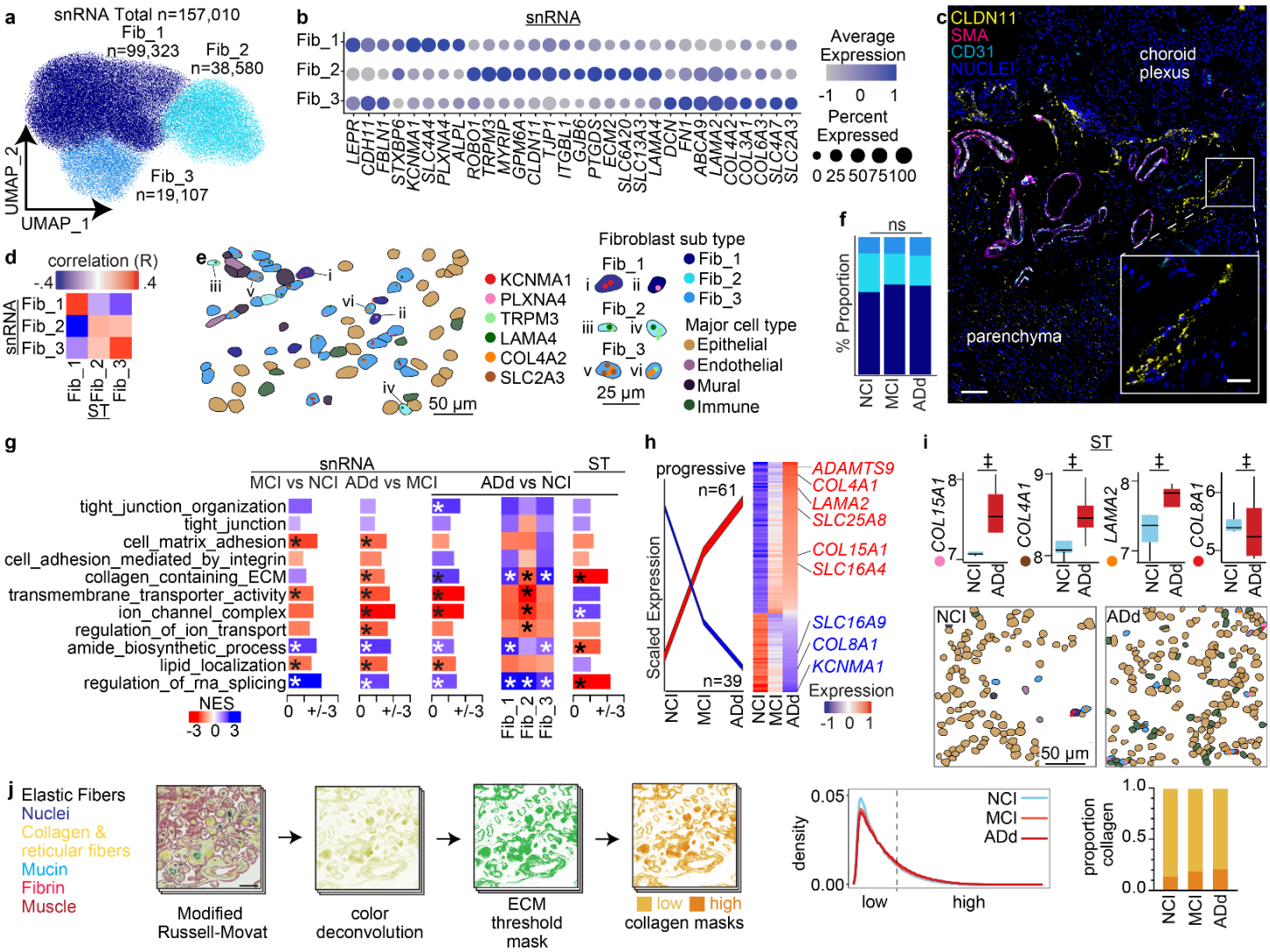

Fig. 4: Fibroblast subtypes and remodeling in Alzheimer's Disease

a, snRNA-seq UMAP projection colored by fibroblast subtypes.

b, Fibroblast subtype-defining marker dot plot (FDR < 0.01, $\log_2$FC > 0.25). See Extended Data Table 19.

c, Multiplexed Opal immunohistochemistry for DAPI, CLDN11, CD31 and SMA, showing localization of CLDN11-positive cells at the boundary between CP and parenchyma. Scale bars = 100µm (overview), 20µm (inset).

d, Pearson correlation of supervised spatial transcriptomics (ST) and snRNA-seq expression among fibroblast subtypes.

e, Spatial localization of fibroblast subtypes overlaid with subtype-defining marker expression; FOV: 2.160. Scale bar: 50µm. Higher magnification on right. Right: Selected examples. Scale bar: 25 µm.

f, Subtype proportions stratified by clinical diagnosis Linear mixed model on proportions (all not significant, FDR > 0.01, ns).

g, Select GO pathways (via fgsea on ranked t statistics) of DEGs throughout clinical disease in snRNA-seq and matched spatial transcriptomics (* FDR < 0.15). See Extended Data Table 20-22.

h, Disease temporal dynamics of DEGs. "progressive" genes: NCI ≠ MCI & ADd and MCI ≠ ADd. Left: line plots indicate the mean of scaled gene expression; line width corresponds to the number of genes following each trajectory. Right: heatmap per stage select genes representing key GO pathways are labelled (nominal p < 0.05, $\log_2$FC > ±0.25, trajectory correlation p < 0.05).

i, Spatial transcriptomic expression of select ECM genes. Upper: boxplots of pseudobulk expression (log_2counts) (median, interquartile range, min/max, ‡ nominal $p < 0.05$); bottom: transcript localization in fibroblasts in NCI FOV #1.86 and ADd FOV #2.119. Scale bar: 50 µm.

j, Upper and lower left: Representative Modified Russel-Movat's stain, deconvoluted yellow (collagen), and ECM threshold mask (< 230 pixel intensity), and high and low collagen masks (230-200, 200-0) (Scale bar: 100µm). Lower middle: averaged distribution of collagen intensity colored by disease stage. Lower right: Stacked barchart of the proportion of high and low collagen by disease stage. n = 8 NCI, 10 MCI, 9 ADd, 5-10 FOVs per subject.

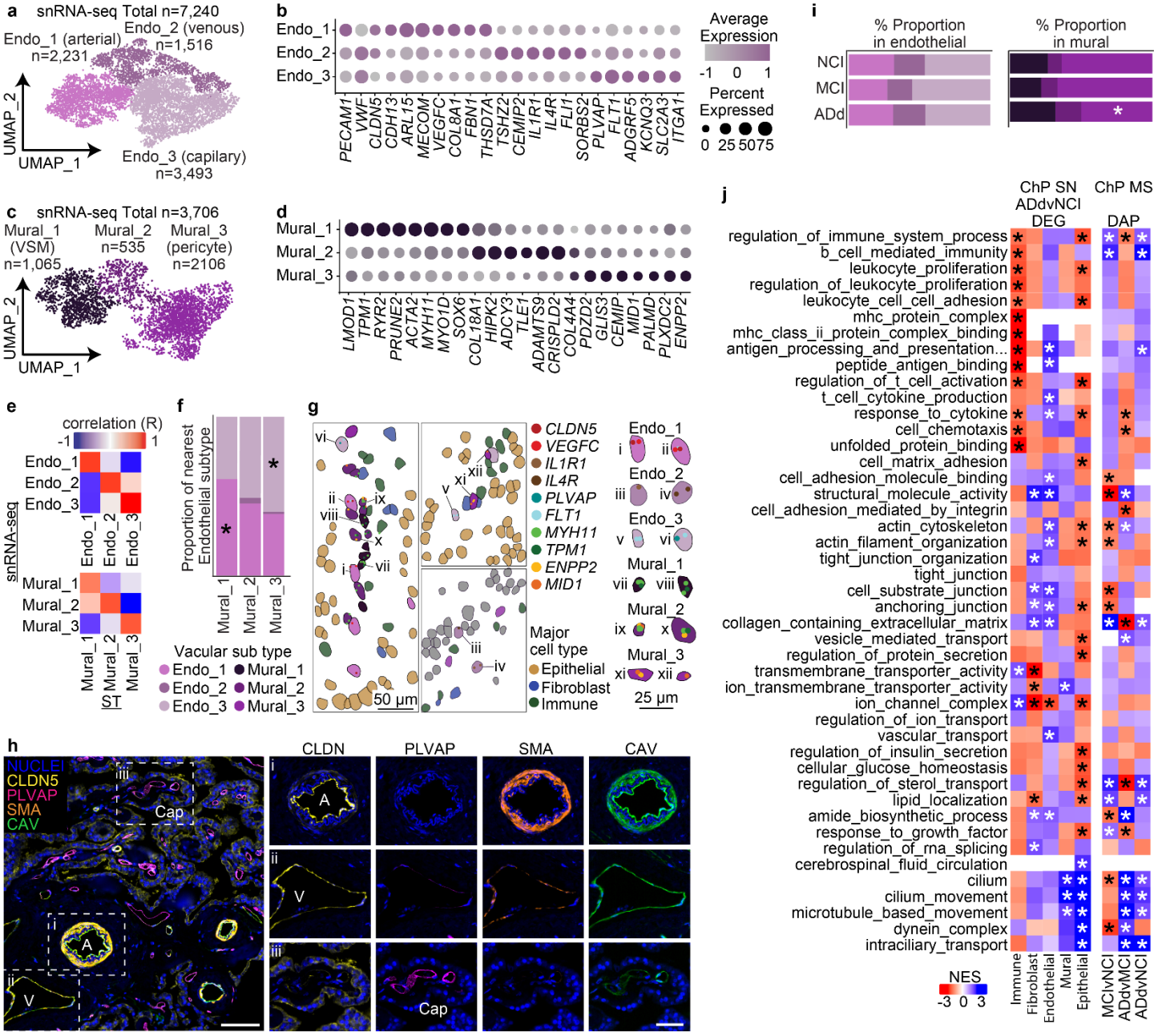

Fig. 5: Endothelial and mural cell dysregulation in Alzheimer's Disease

a, & c, snRNA-seq UMAP colored by endothelial (a) and mural (c) subtypes.

b, & d, Endothelial (b) and mural (d) subtype-defining marker dot plot (FDR < 0.01, $\log_2$FC > 0.25). See Extended Data Tables 22-23.

e, Pearson correlation of supervised spatial transcriptomics (ST) to snRNA-seq expression pooled among endothelial (upper) and mural (lower) subtypes.

f, Proportion of nearest endothelial subtype across Mural subtypes. Linear mixed model on proportions (* $p < 0.05$).

g, Spatial localization of endothelial and mural subtypes overlaid with subtype-defining marker expression; FOV: 1.186; Scale bar: 50µm. Right: Selected examples. Scale bar: 25 µm.

h, Phenocycler fusion immunofluorescence of endothelial (CLDN5, CAV, PLVAP) and mural (SMA) with DAPI. Capillary (Cap), arterial (A), and vascular venous(V) structures indicated and split by stain on right.

i, Endothelial (left) and mural (right) subtype proportions stratified by clinical diagnosis. Scale bars = 100µm (overview), 50µm (insets); Mural_3 * FDR < 0.01, others not significant.

j, Select GO pathways (via fgsea on ranked t statistics) of ADd vs NCI DEGs across all major cell types matched to mass spectrophotometry proteomics throughout clinical disease (*FDR < 0.15). See Extended Data Tables 24-28.

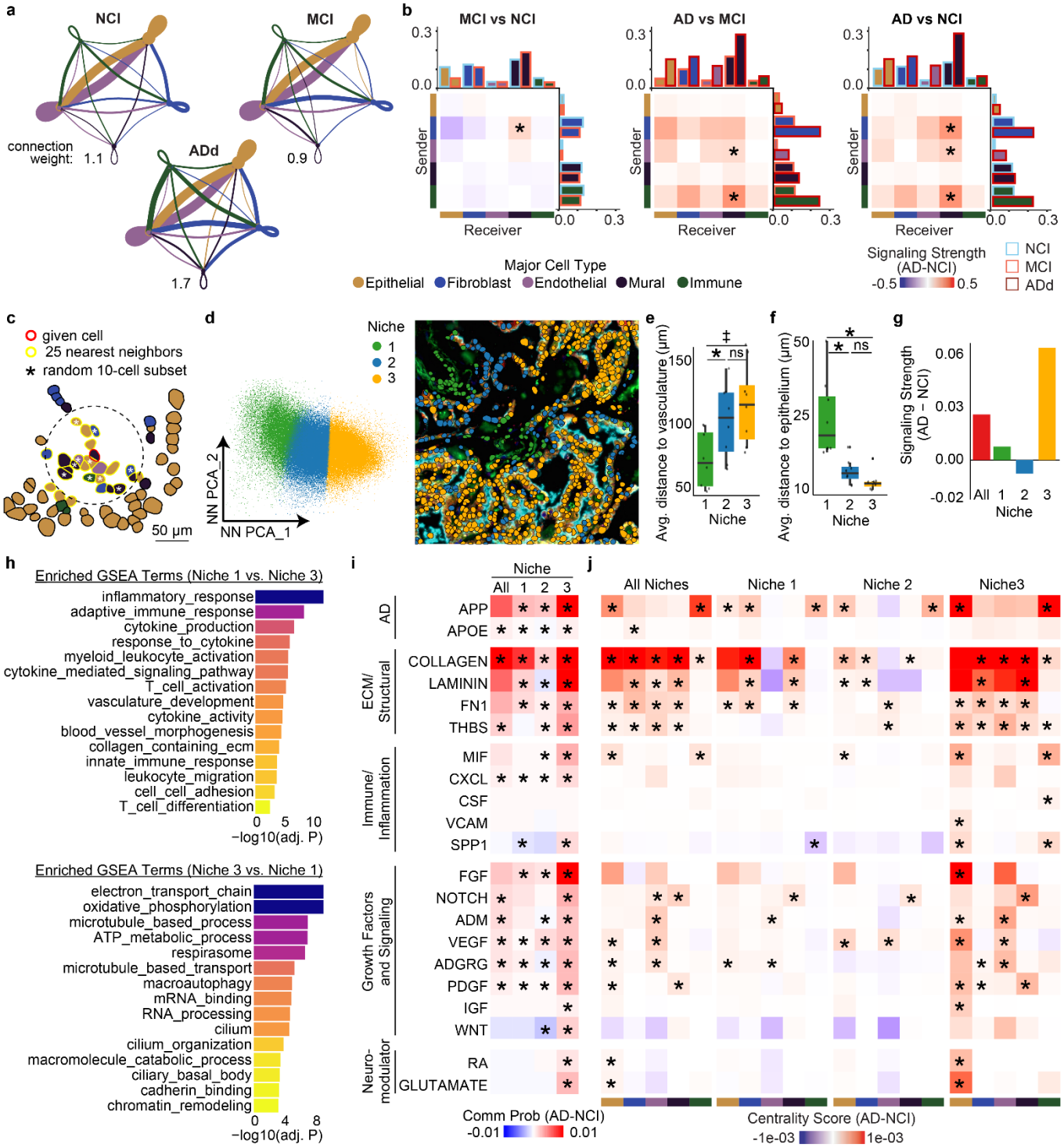

Fig. 6: Altered CP intercellular communication in AD

a, AD differential CellChat inferred communication weights between major cell types throughout clinical disease progression in snRNA-seq.

b, AD differential CellChat net probability (CellChat net$prob) heatmaps among all ligand-receptor pairs in each colored sender-receiver pair (* $p < 0.05$).

c, Partial field of view (FOV #1.89), with cells colored by major cell type, to illustrate the nearest neighbor analysis approach. For each cell (e.g. red-outlined cell), a neighborhood transcriptome profile is calculated by averaging expression of a random 10-cell subset (white asterisks) of its 25 nearest neighbors (yellow-outline).

d, Left: UMAP representation of neighborhood expression matrix colored by cluster (k-means = 3). Right: spatial plot of FOV #1.89, with cells colored by niche identity overlaid on immunofluorescent image.

e-f, Boxplots of average cell to cell distances per niche to the nearest target cell type(s): Endothelial or Mural cell for (e), Epithelial cell for (f). Pairwise Wilcoxon tests with BH correction between niche (* $p < 0.05$, ‡ $p=0.07$, ns: not significant).

g, CellChat normalized AD-differential signaling strength bar charts.

h, Bar charts of select GO terms with positive enrichment (via fgsea on ranked t statistic) for niche 1 (upper) and niche 3 (lower).

i, Interaction probability heatmap of select AD-differential CellChat pathways, for either the full or niche-specific datasets (* $p < 0.05$).

j, For the same pathways in (i), AD-differential signaling split by colored cell types, for either the full or niche-specific datasets (* $p < 0.05$)

Extended Data Figures

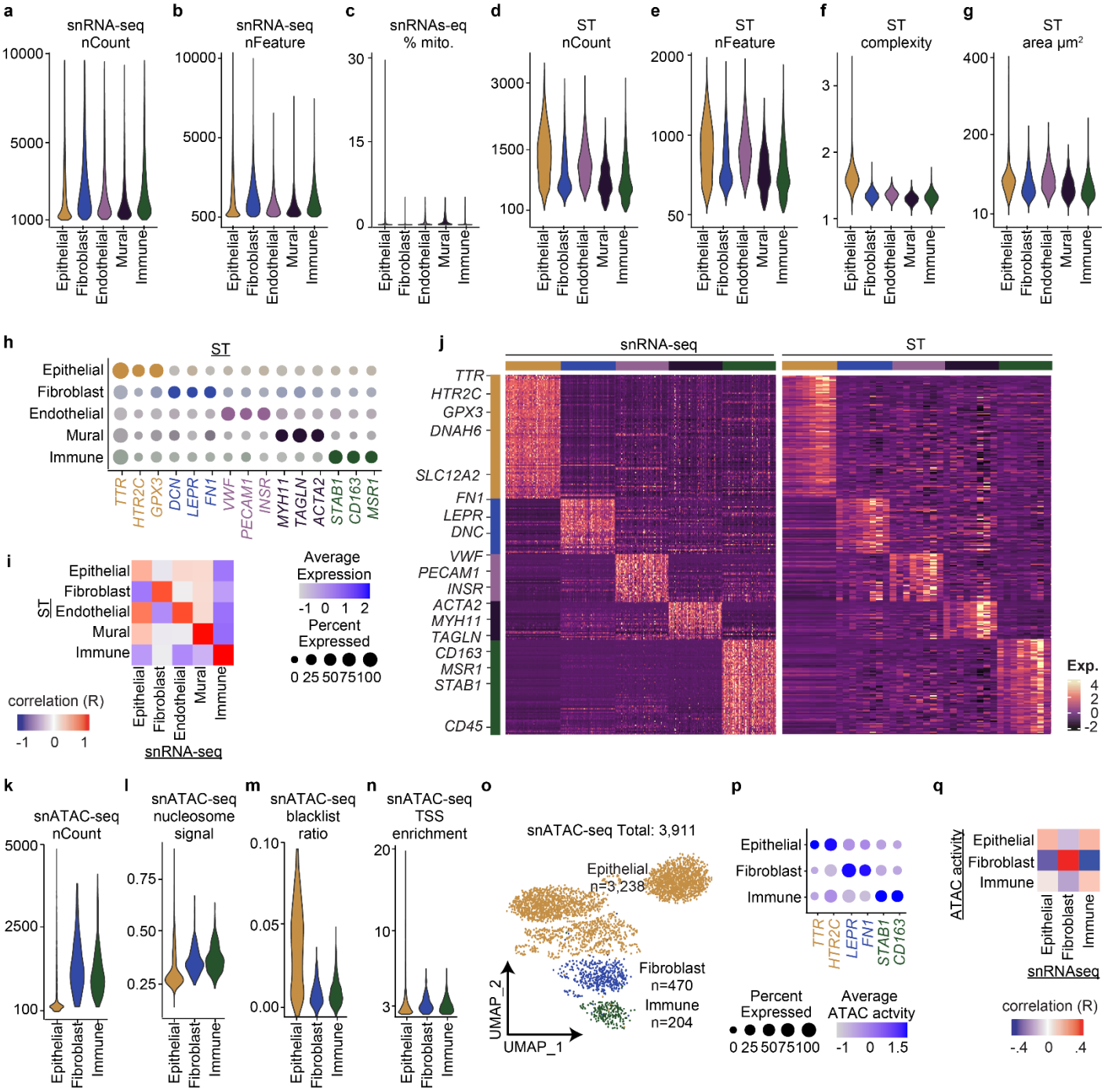

Extended Data Fig. 1: QC and cell-type validation across snRNA-seq, ST ad snATAC-seq

a–c, Total RNA counts(a), number of detected features (b), and Mitochondrial read percentage (c) violin plots per snRNA-seq subtype.

d–g, Total RNA counts (a), number of detected features (b), segmented cell area (µm²; c) and complexity (d) violin plots per spatial transcriptomic (ST) subtype.

h, Unsupervised spatial transcriptomic confirmation of canonical marker expression dot plot across cell clusters. See Extended Data Table 4.

i, Pearson correlation of ST to RNA expression by major cell type..

j, Heatmap of pseudobulked marker gene expression (z-score) identified in snRNA-seq (limma; FDR < 0.01, $\log_2$FC > 0.25). Heatmap of the same gene set in pseudobulked ST.

k-n, Total peaks counts (k), nucleosome_signal (l), blacklist_ratio (m), and TSS_enrichment (n) violin plots per snATAC-seq subtype.

o, UMAP projection of major celltypes with cell counts indicated.

p, Unsupervised snATAC-seq confirmation of canonical marker expression dot plot across cell clusters. See Extended Data Table 6.

q, Pearson correlation of chromatin accessibility to RNA expression pooled among major cell types.

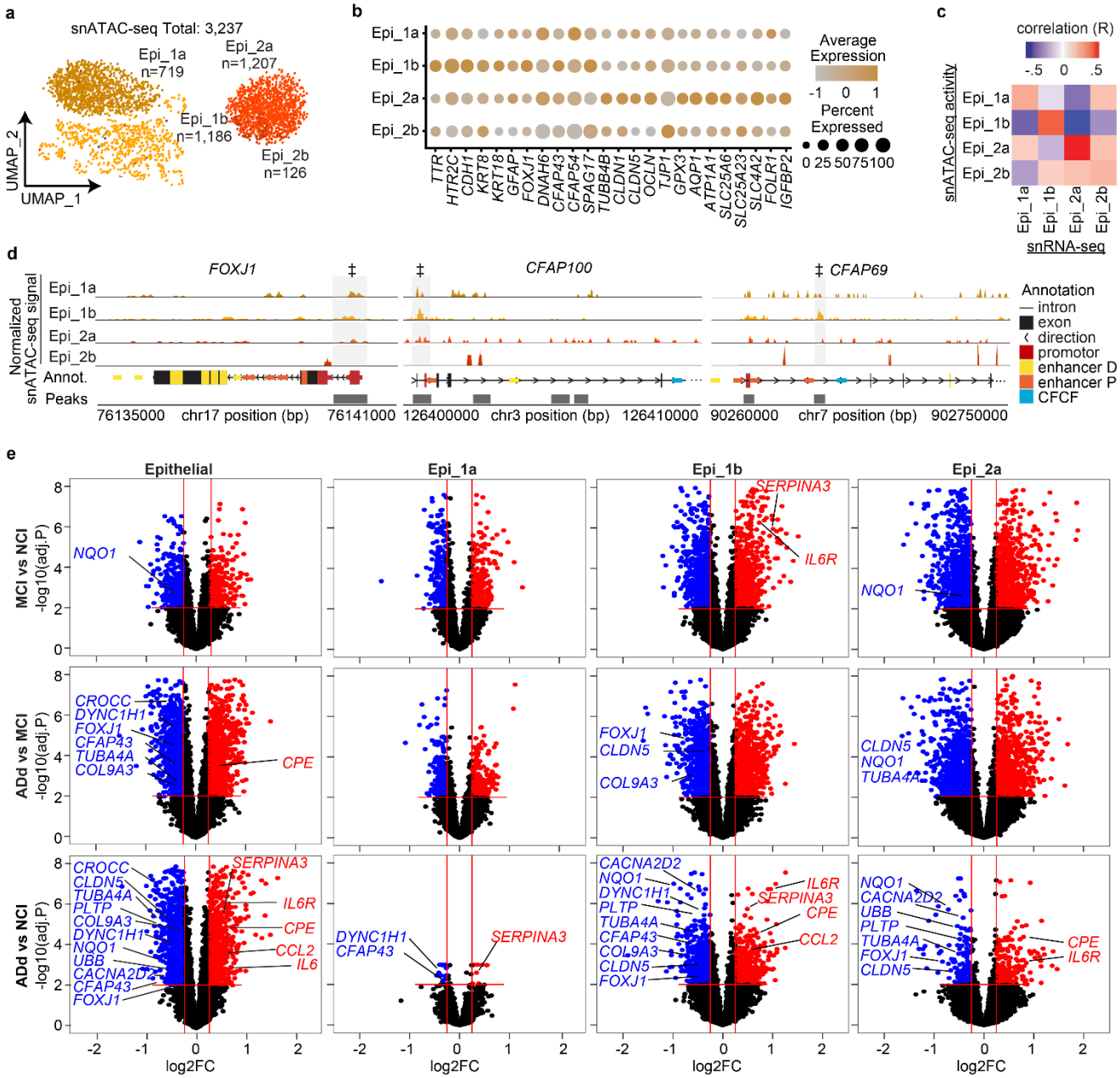

Extended Data Fig. 2: Epithelial cell subtypes defined by snATAC-seq and differential gene expression across disease stages

a, snATAC-seq UMAP colored by epithelial subtype.

b, Unsupervised snATAC-seq epithelial subtype-defining marker dot plot (FDR < 0.01, $\log_2$FC > 0.25). See Extended Data Table 9.

c, Pearson correlation of chromatin accessibility (ATAC activity) to RNA expression pooled among epithelial subtypes.

d, Differentially accessible chromatin peaks for select cilia genes per epithelial subtypes (‡ p<0.05). Genome specific annotations and accessible peaks are shown below.

e, snRNA-seq **e**pithelial and **s**ub type * disease specific DEG volcano plots. Select genes representing key GO pathways are labelled (all FDR < 0.01 and $\log_2$ fold change > ±0.25).

f, Scatter plots contrasting t-statistics from differential gene expression analysis between clinical stages (MCI vs NCI and ADd vs NCI), Select genes representing key GO pathways are labelled (all FDR < 0.01 and $\log_2$ fold change > ±0.25).

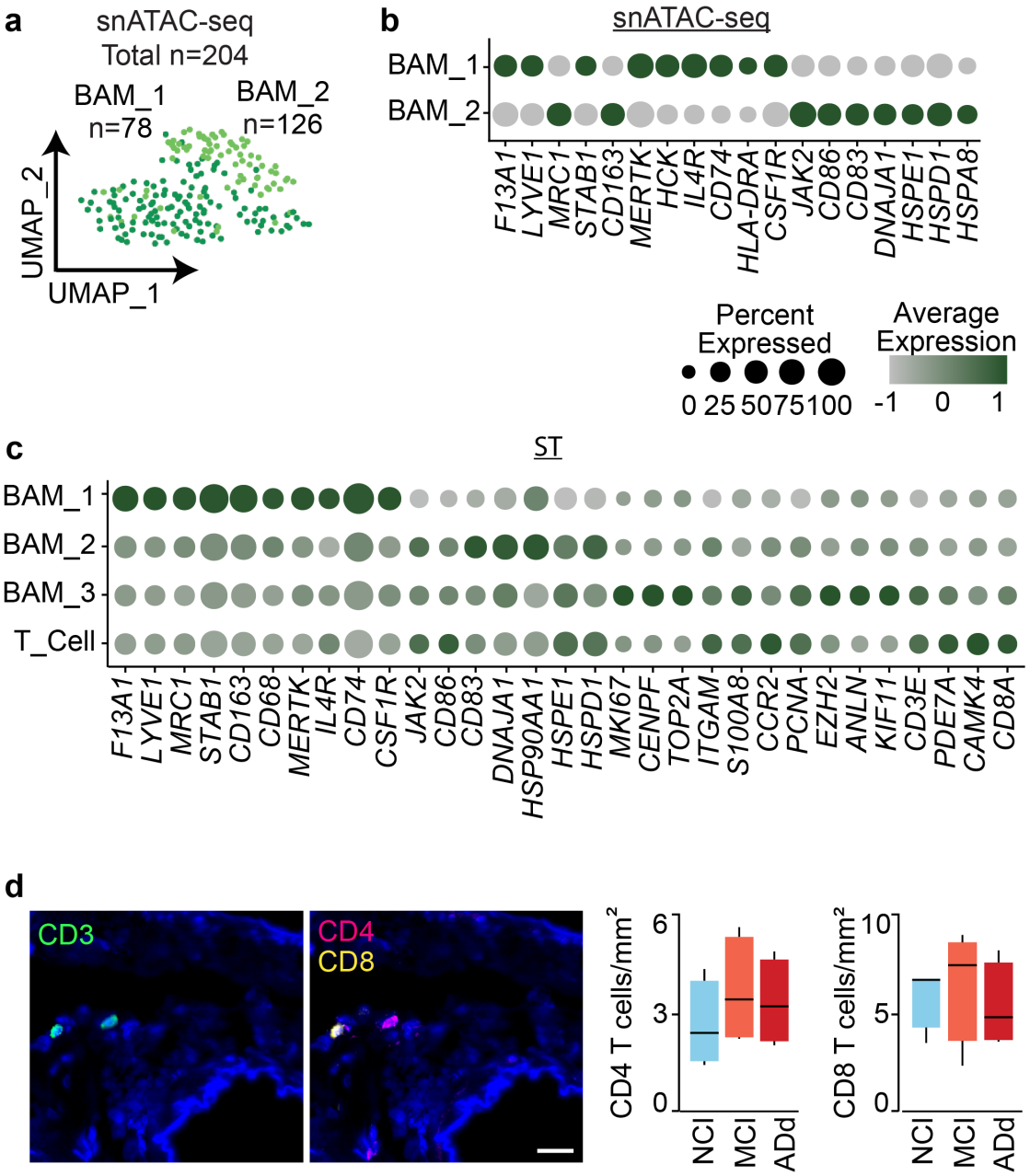

Extended Data Fig. 3: Immune cell subtypes defined by snATAC-seq and ST

a, snATAC-seq UMAP colored by immune subtypes.

b, Unsupervised snATAC-seq immune subtype-defining marker dot plot. See Extended Data Table 16.

c, Supervised spatial transcriptomics (ST) immune subtype-defining marker dot plot.

d, CD4 and CD8 staining and quantifications across NCI, MCI and AD groups.

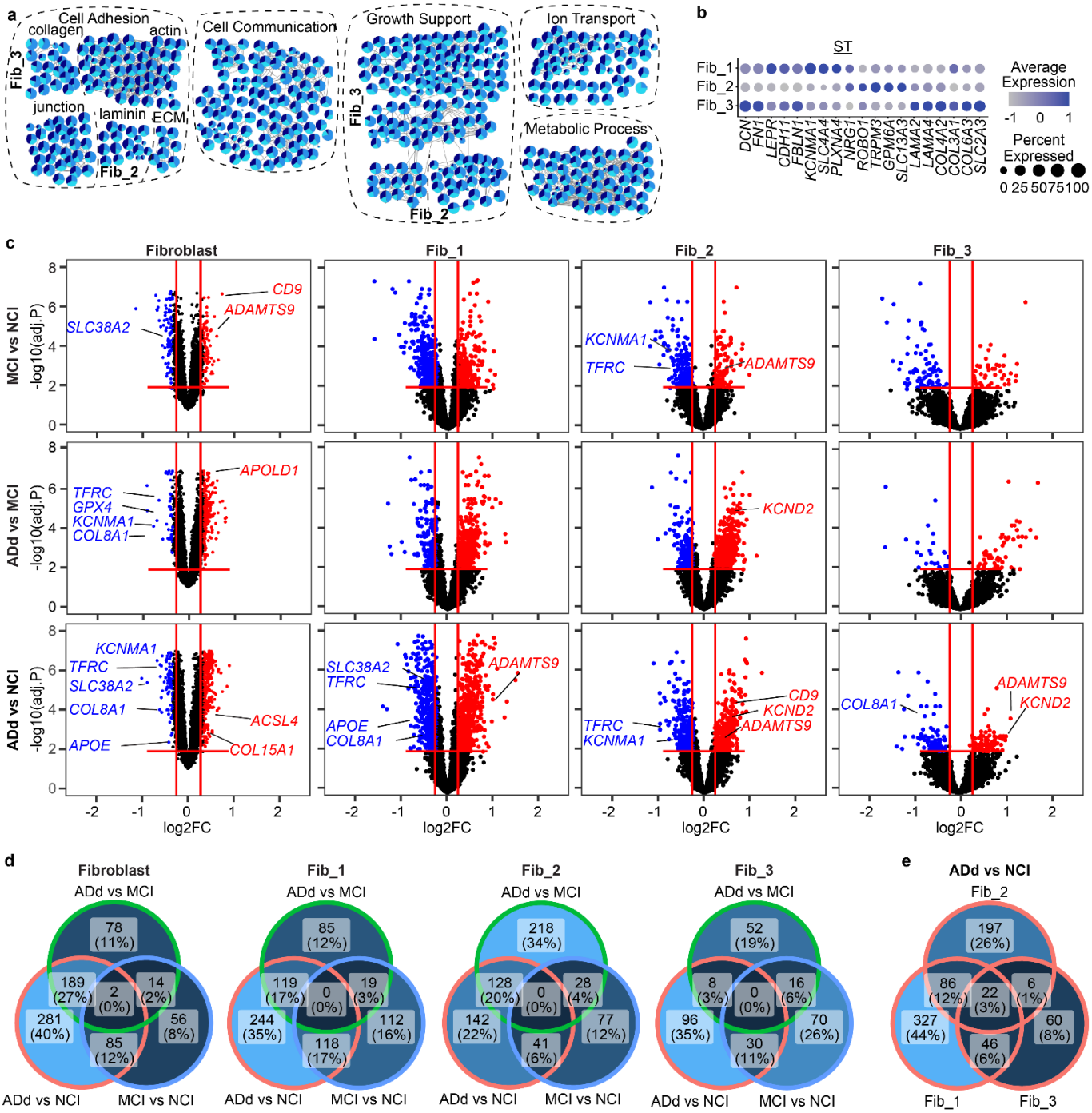

Extended Data Fig. 4: Fibroblast subtype-resolved differential gene expression across disease stages

a, Fibroblast subtype GO enrichment network plot (ClueGO on subtype-defining markers) grouped by functional category.

b, Supervised spatial transcriptomics (ST) fibroblast subtype-defining marker dot plot.

c, snRNA-seq fibroblast and sub type * disease specific DEG volcano plots. Select genes representing key GO pathways are labelled (all FDR < 0.01 and $\log_2$ fold change > ±0.25).

b, Overlap of differentially expressed genes across subtypes and disease stages.

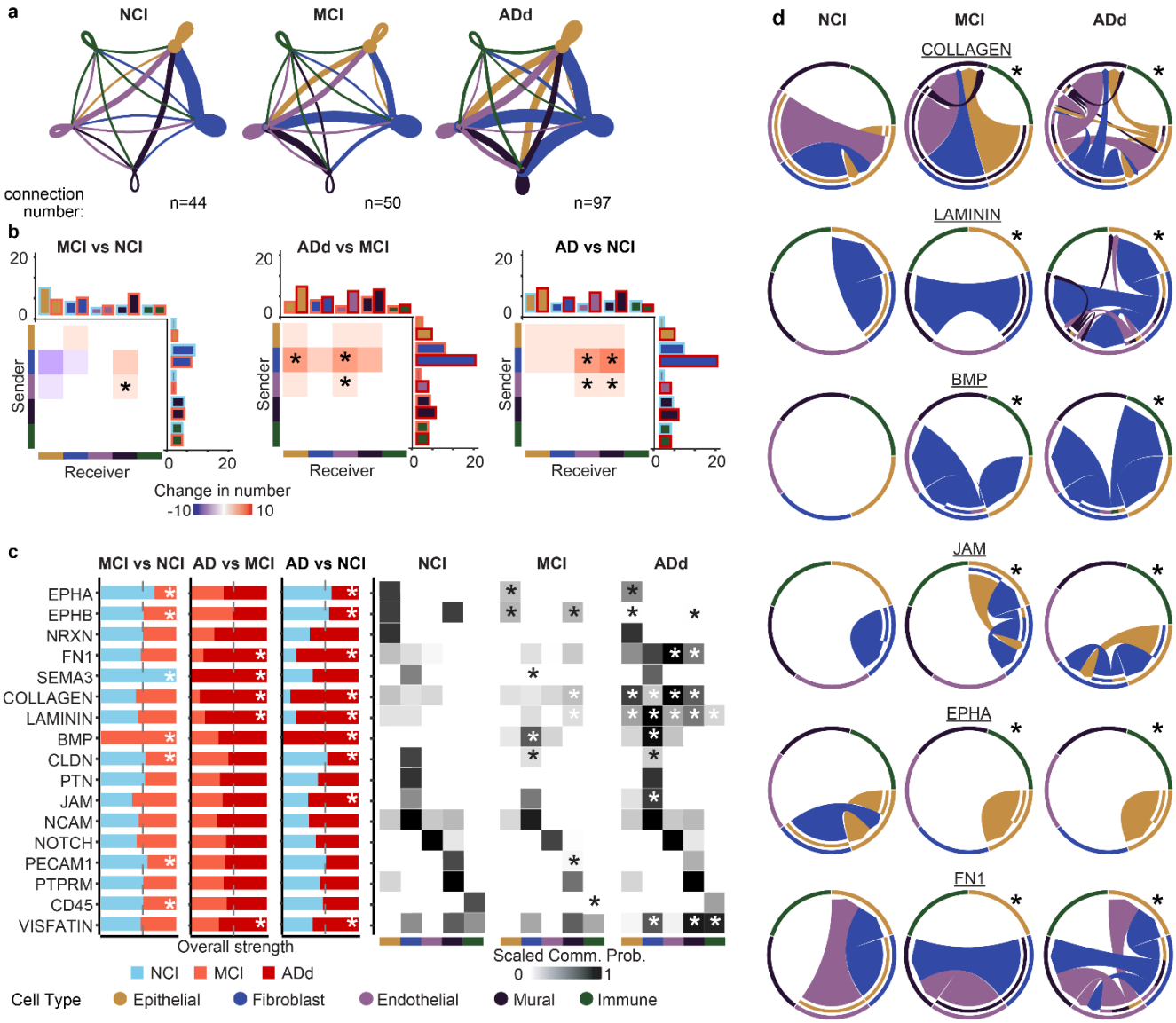

Extended Data Fig. 5: CellChat analysis of snRNA-seq data reveals altered CP intercellular communication in AD

a, Differential CellChat inferred communication number between major cell types throughout clinical disease progression in snRNA-seq.

b, AD differential CellChat communication number heatmaps among all ligand-receptor pairs in each colored sender-receiver pair (* $p < 0.05$).

c, Select signaling pathways mediating differential intercellular communication throughout clinical disease progression. Left: Total signaling strength histogram. Right: Scaled communication probability per cell type (* $p < 0.05$). See Extended Data Table 29.

d, Selected chord diagrams of intercellular signaling between major cell types throughout clinical disease progression (* $p < 0.05$).

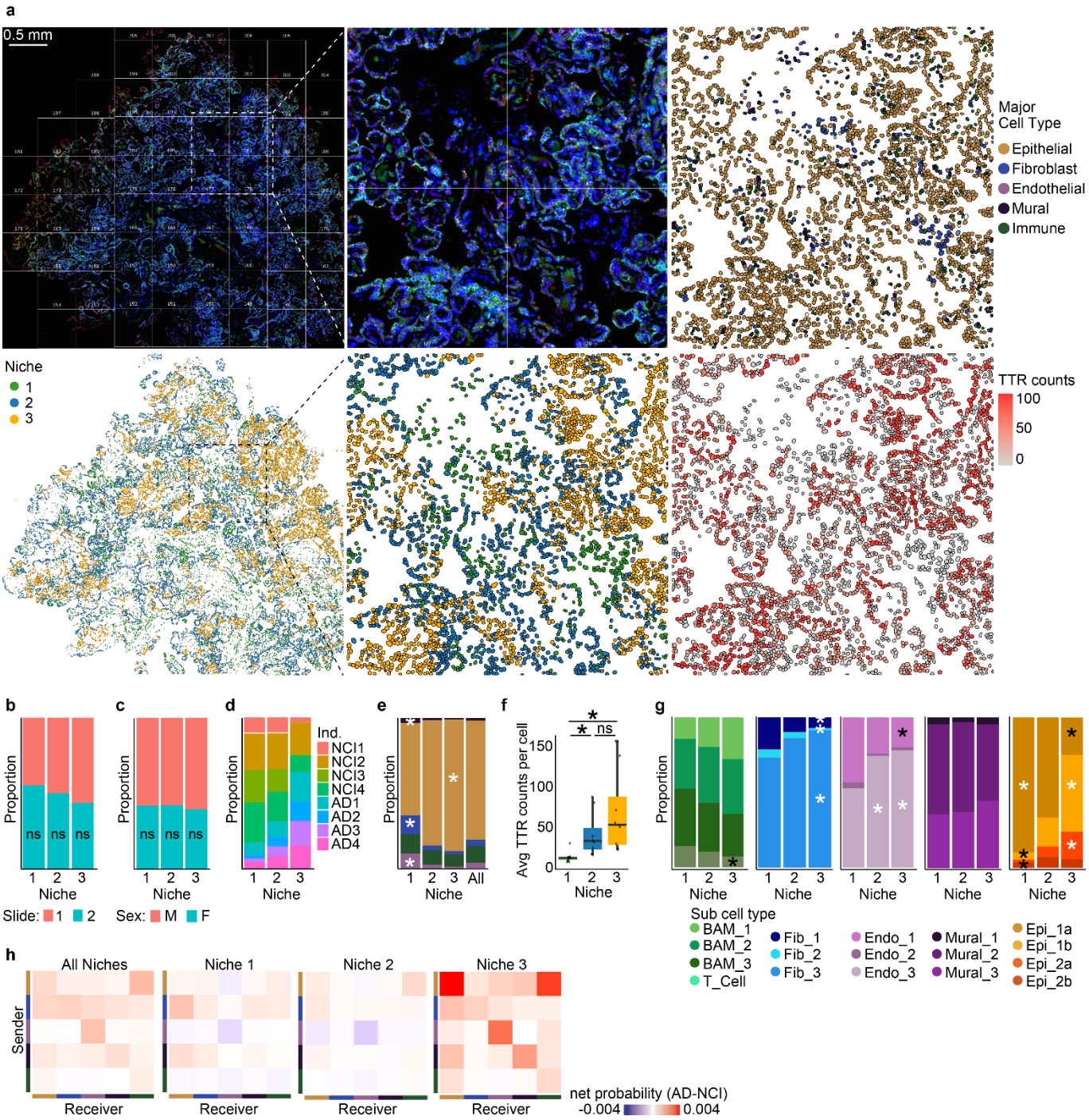

Extended Data Fig. 6: Niche-specific communication changes in Alzheimer's disease

a, Example tissue section immunofluorescent stain (upper left) colored by niche (lower left). Middle: Higher magnification of 4 FOVs. Upper right: Major cell type annotation. Lower left: TTR counts per cell type.

b-e, Stacked bar charts showing proportion of slide (b), sex (c), individual (d), major cell type (e) per niche. Linear mixed model on proportions (Mural, Fibroblast and Endothelial in niche 1, Epithelial in niche 3 * FDR < 0.05, ns: not significant).

f, Boxplot shows individual- and niche-specific pseudobulk expression of TTR (* p <0.001, ns: not significant).

g, Stacked bar charts showing subtype proportions per niche (* FDR < 0.05).

h, AD differential CellChat net probability (CellChat net$prob) heatmaps among all ligand-receptor pairs in each colored sender-receiver pair, for all cells (left), or subset by niche.

Extended Data Tables

1228 **Extended Data Table 1**. Patient metadata

1229 **Extended Data Table 2**. SN major celltype limma and GO

1230 **Extended Data Table 3**. SN major and sub proportions and limma

1231 **Extended Data Table 4**. ST major celltype limma and GO

1232 **Extended Data Table 5**. ST major and sub proportions and limma

1233 **Extended Data Table 6**. ATAC major celltype limma and GO

1234 **Extended Data Table 7**. Epi SN subcelltype limma and GO

1235 **Extended Data Table 8**. Epi ST subcelltype limma and GO

1236 **Extended Data Table 9**. Epi ATAC subcelltype limma and GO

1237 **Extended Data Table 10**. Epi SN major and sub cogdx and pattern limma and GO

1238 **Extended Data Table 11**. Epi SN major and sub cog_dec limma and GO

1239 **Extended Data Table 12**. Epi ST major cogdx limma and GO

1240 **Extended Data Table 13**. Epi ATAC TF motifs subtype limma

1241 **Extended Data Table 14**. CSF proteomic DEG limma and GO

1242 **Extended Data Table 15**. Imm SN subcelltype limma and GO

1243 **Extended Data Table 16**. Imm ATAC subcelltype limma and GO

1244 **Extended Data Table 17**. Imm SN major and sub cogdx and pattern limma and GO

1245 **Extended Data Table 18**. Imm ST major and sub cogdx

1246 **Extended Data Table 19**. Fib SN subcelltype limma and GO

1247 **Extended Data Table 20**. Fib SN major and sub cogdx and pattern limma and GO

1248 **Extended Data Table 21**. Fib ST major cogdx limma and GO

1249 **Extended Data Table 22**. Endo SN subcelltype limma and GO

1250 **Extended Data Table 23**. Mural SN subcelltype limma and GO

1251 **Extended Data Table 24**. Endo SN major cogdx limma and GO

1252 **Extended Data Table 25**. Endo ST major cogdx limma and GO

1253 **Extended Data Table 26**. Mural SN major cogdx limma and GO

1254 **Extended Data Table 27**. Mural ST major cogdx limma and GO

1255 **Extended Data Table 28**. Proteomic DEG limma and GO

1256 **Extended Data Table 29**. SN and ST CellChat net_pathways and limma results

1257 **Extended Data Table 30**. Canonical markers and references